Mechanical Systems and Signal Processing 133 (2019) 106273

Contents lists available at ScienceDirect

Mechanical Systems and Signal Processing

journal homepage: www.elsevier.com/locate/ymssp

Asymptotic identification uncertainty of close modes in Bayesian operational modal analysis

Siu-Kui Au [a,*], James M.W. Brownjohn [b,c]

[a] School of Civil and Environmental Engineering, Nanyang Technological University, 50 Nanyang Avenue, Singapore 639798, Singapore
[b] Director, Full Scale Dynamics Limited, The Innovation Centre, 217 Portobello, Sheffield S1 4DP, UK
[c] College of Engineering Mathematics and Physical Sciences (CEMPS), University of Exeter, Harrison Building, Exeter EX4 4QF, UK

ARTICLE INFO

Article history:
Received 18 August 2018
Received in revised form 16 July 2019
Accepted 24 July 2019

Keywords:
Ambient modal identification
Close modes
Fisher Information Matrix
Operational modal analysis
Uncertainty laws

ABSTRACT

Close modes are not typical subjects in operational modal analysis (OMA) but they do occur in structures with modes of similar dynamic properties such as tall buildings and towers. Compared to well-separated modes they are much more challenging to identify and results can have significantly higher uncertainty especially in the mode shapes. There are algorithms for identification (ID) and uncertainty calculation but the value itself does not offer any insight on ID uncertainty, which is necessary for its management in ambient test planning. Following a Bayesian approach, this work investigates analytically the ID uncertainty of close modes under asymptotic conditions of long data and high signal-to-noise ratio, which are nevertheless typical in applications. Asymptotic expressions for the Fisher Information Matrix (FIM), whose inverse gives the asymptotic 'posterior' (i.e., given data) covariance matrix of modal parameters, are derived explicitly in terms of governing dynamic properties. By investigating analytically the eigenvalue properties of FIM, we show that mode shape uncertainty occurs in two characteristic types of mutually uncorrelated principal directions, one perpendicular (Type 1) and one within the 'mode shape subspace' spanned by the mode shapes (Type 2). Uncertainty of Type 1 was found previously in well-separated modes. It is uncorrelated from other modal parameters (e.g., frequency and damping), diminishes with increased data quality and is negligible in applications. Uncertainty of Type 2 is a new discovery unique to close modes. It is potentially correlated with all modal parameters and does not vanish even for noiseless data. It reveals the intrinsic complexity and governs the achievable precision limit of OMA with close modes. Theoretical findings are verified numerically and applied with field data. This work has not reached the ultimate goal of 'uncertainty law', i.e., explicitly relating ID uncertainty to test configuration for understanding and test planning, but the analytical expressions of FIM and understanding about its eigenvalue properties shed light on possibility and provide the pathway to it.

1. Introduction

Modal identification (ID) aims at identifying the in-situ modal properties, e.g., natural frequencies, damping ratios and mode shapes, of a structure based on vibration data [1–3]. 'Well-separated' modes, i.e., a single mode dominating its own

* Corresponding author at: Formerly with Institute for Risk and Uncertainty and School of Engineering, University of Liverpool, Harrison Hughes Building, Brownlow Hill, Liverpool L69 3GH, UK.
E-mail addresses: ivanau@ntu.edu.sg, siukuiau@liverpool.ac.uk (S.-K. Au), J.Brownjohn@Exeter.ac.uk (J.M.W. Brownjohn).

https://doi.org/10.1016/j.ymssp.2019.106273
0888-3270/

resonance band, are typical but 'close modes' do occur. The latter are often referred as modes whose natural frequencies are so close that their resonance bands overlap, e.g., visually in the power spectral density (PSD) or singular value (SV, i.e., eigenvalue of PSD matrix) spectrum of data. Fig. 1 gives an example of triaxial ambient acceleration data recorded on a tall building roof. The resonance band indicated by the horizontal bar contains two close modes that are translational in nature.

Close modes most typically occur in various forms of tower having two or more horizontal axes of symmetry, e.g., tall buildings [4,5], telecommunication (guyed) masts and freestanding lattice towers [6], cylindrical chimneys [7,8], space launchers [9] and lighthouses [10]. For tall buildings the stiffness and mass properties along two principal directions can be very similar by design, whereas for the other structures symmetry and resultant close modes are a natural consequence of the structural form adopted to fulfil their function against environmental (usually wind) loads. Identifying close modes is important for these structures because they are the effect of subtle differences in stiffness and mass distribution within the almost symmetric structure. Close modes can be found by chance in other structures, such as suspension bridges, e.g., Humber Bridge [11] where closeness of torsional and vertical mode frequencies can affect in-wind dynamics by aeroelasticity.

Unlike well-separated modes, close modes are much more challenging in terms of prediction, ID formulation, computational algorithm and ID uncertainty. Theoretically, for modes with identical frequencies, only the subspace spanned by their mode shapes, i.e., 'mode shape subspace' (MSS), rather than the individual ones can be uniquely determined. This is because any linear combination of mode shapes with identical frequencies satisfies the same eigenvalue equation and hence is also a mode shape. Mode shapes with close frequencies have high sensitivity especially within the MSS to perturbations in structural properties [12,13]. A higher order MAC (modal assurance criterion) was defined for close modes in terms of their MSS [14]. The entangling of modal dynamics renders intuition about their behaviour somewhat obscured. In operational modal analysis (OMA) that aims at modal ID based on output-only data, well-separated modes can often be identified with reliable quality from data with reasonable signal-to-noise (S/N) ratio but the same is not true for close modes. Identified mode shapes are inevitably limited to the measured DOFs (degrees of freedom) and so they need not be orthogonal. Many OMA methods only calculate 'operational deflection shapes' for close modes from matrix decomposition (so necessarily orthogonal) rather than the ones in structural dynamics theory. Identifying the mode shapes of close modes requires resolving their coordinates with respect to (w.r.t.) the orthogonal basis spanning their subspace, which are entangled with other modal properties and require sophisticated iterative algorithms, e.g., [15].

Significant variability especially in the identified mode shapes can occur from data sets of apparently similar quality. This is often attributed to the sensitivity to underlying properties, e.g., [16] (Section 5.3.3) and [17]; but the authors are not aware of any direct account of ID uncertainty. Calculating ID uncertainty for given data is another level of sophistication beyond ID algorithm, for which methods are available depending on the particular modal ID algorithm adopted, e.g., Stochastic Subspace Identification [18–20] and Bayesian OMA (BAYOMA) [21,22]. However, the values of the uncertainty bounds do not allow one to understand ID uncertainty and how it depends on the test configuration. The latter aims add to yet another level of challenge that appears intractable, considering the already high sophistication in the ID and uncertainty calculation algorithms; and may not even be possible depending on the intrinsic nature of the problem. Remarkably, recent BAYOMA research on well-separated modes [23] reveals the possibility of insightful asymptotic expressions for the ID uncertainty in terms of test configuration for long data, small damping and high S/N ratio, which are nevertheless typical in applications. Such expressions are collectively referred as 'uncertainty law'.

This work takes on the challenge of developing uncertainty law for close modes. It has not reached the level of insight that has been achieved for well-separated modes but it reports two milestones that are critical to the development and reveal the existence of mathematical beauty. The first milestone is the high S/N asymptotic expression for the Fisher Information Matrix (FIM) explicitly in terms of modal properties in the problem; inverting the FIM gives the asymptotic ID uncertainty (Section 4). The second milestone is the discovery of mutually uncorrelated principal directions of mode shape uncertainty

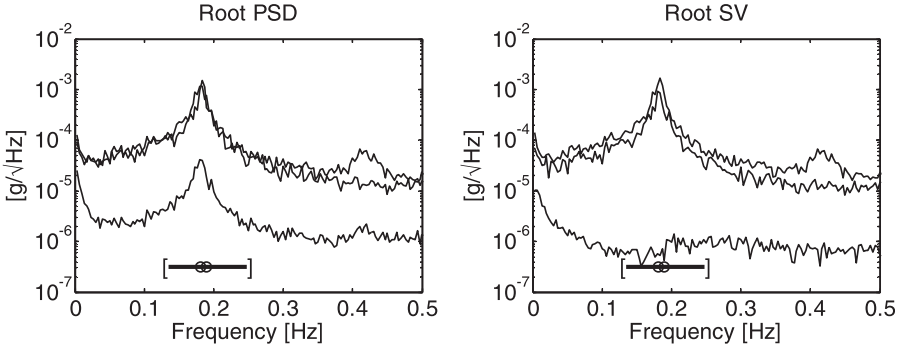

Fig. 1. Root PSD and root SV spectrum of triaxial acceleration data on tall building roof. In the root PSD plot, the top two lines are x and y, bottom line is z. Bar below peak shows band for modal ID.

through analytical study on the eigenvalue properties of the asymptotic FIM, reducing the complexity of problem so that it does not grow with the number of measured DOFs. These contributions will be explained qualitatively in Section 2 and technically in Section 5 after overview of theoretical framework in Sections 3 and 4. Section 6 outlines the theory that establishes the first milestone with details provided in Appendices A–C. Sections 7 and 8 deliver the second milestone. The theoretical findings are verified and applied in Section 10. The paper is concluded in Section 11. To facilitate reading, Table 1 lists the abbreviations used in this work.

2. Key findings in qualitative terms

To have an appreciation of key discoveries, consider modal ID of m close modes with ambient triaxial data, i.e., the number of measured DOFs is $n = 3$. The basic assumptions in the ID model (as in BAYOMA) include linear dynamics with classically damped modes, stationary modal excitations with constant PSD matrix within resonance band and stationary noise, independent and identically distributed (i.i.d.) among measured DOFs with a constant PSD within the resonance band. Data is assumed to be sufficiently long in the sense that the number of FFT points in the resonance band is large compared to 1 (see Section 4); and has high S/N ratio (see (47)). Fig. 2 conveys the new knowledge generated. In each case, the big arrow pointing from the origin (black dot) shows the mode shape $\boldsymbol{\varphi}_i$ normalised to have unit length. The smaller arrows at the larger arrow tip show different directions of ID uncertainty. The case of $m = 1$ (well-separated modes) represents what is currently understood [23]. In this case the uncertainties are all along directions perpendicular to the mode shape. There are $n - m = 3 - 1 = 2$ such directions, depicted by y and z in the figure; the plane in red covers all possible directions. There is no uncertainty along the mode shape direction because the length is constrained to 1. The uncertainties along the y and z direction are uncorrelated. They are not correlated with other modal properties (e.g., frequency, damping) either. Their size diminishes with increased data quality and vanishes for noiseless data. In applications it is typically small and not of concern.

The cases for $m = 2$ and 3 are close modes, where the new knowledge contributes. In this case there are two types of uncertainties, one perpendicular to the mode shapes (Type 1) and the other within the plane or space they span (Type 2). When $m = 2$, the two mode shapes $\boldsymbol{\varphi}_1$ and $\boldsymbol{\varphi}_2$ span over the blue plane (2-D) and there is only one direction (z) perpendicular to it. In addition to the small red arrow, there is now uncertainty within the blue plane, denoted by the small blue arrow along the tangential direction of the unit circle. So far recognising these two types of uncertainty may appear to be mere geometry. The new discovery is that the uncertainties along the two small red arrows are of a similar nature as their counterpart for $m = 1$, i.e., not correlated with other modal properties and diminishing with increased data quality. More remarkable is the uncertainty along the small blue arrows. It is uncorrelated from the uncertainty of the red arrows but is generally correlated with all other modal properties. It prevails even for noiseless data and hence represents the achievable ID precision unique to OMA of close modes. When $m = 3$ the mode shapes span over a 3-D space and there is no direction perpendicular to all mode shapes (so no red arrows). All uncertainties are along the small blue directions within the MSS.

The above picture is for illustration only. The theory developed in this work applies to general n and m with no regards to spatial context; and the uncertainties can be quantified with analytical expressions (see Table 2). It is applicable regardless of how close the modes are. All statements will be established mathematically in the context of Bayesian inference and asymptotics. Up to modelling assumptions of classically damped dynamics and stochastic stationary data, the limit on ID uncertainty is what can be best achieved regardless of the modal ID method adopted, because a Bayesian approach processes information from data consistent with probability and modelling assumptions.

Table 1
Abbreviations used in this work.

Short	Long
BAYOMA	Bayesian Operational Modal Analysis
c.o.v.	Coefficient of variation
DOF	Degree of freedom
FFT	Fast Fourier Transform
FIM	Fisher Information Matrix
i.i.d.	Independent and identically distributed
ID	Identification
MAC	Modal assurance criterion
MPV	Most probable value
MSS	mode shape subspace
OMA	Operational Modal Analysis
PSD	Power spectral density
S/N	signal-to-noise
SV	Singular value
w.r.t.	with respect to

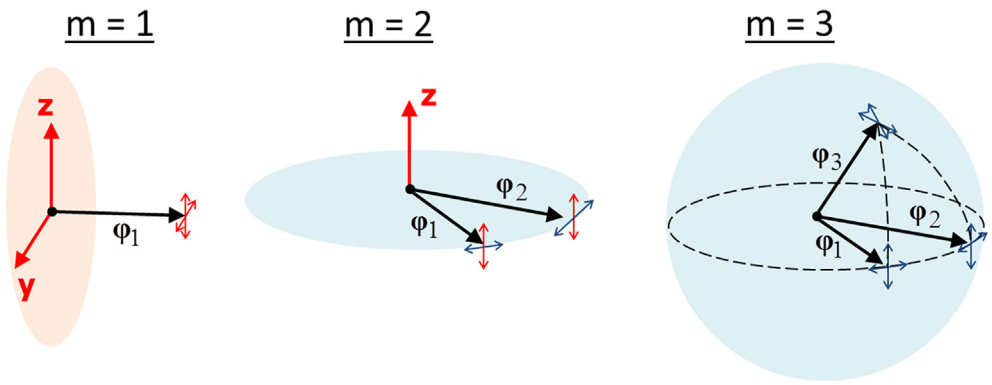

Fig. 2. Directions of mode shape uncertainty (small arrows at big arrow tip) for $n = 3$ measured DOFs and different number of close modes m. Uncertainty along small red arrows (Type 1) is perpendicular to mode shape subspace (MSS) and vanishes for noiseless data. Uncertainty along small blue arrows (Type 2) is within MSS and prevails even for noiseless data. See also Fig. 3. (For interpretation of the references to colour in this figure legend, the reader is referred to the web version of this article.)

Table 2
Asymptotic expressions for FIM for high S/N ratio. '$x, y = f, \zeta, \boldsymbol{S}$' denotes that x and y are frequency, damping or real/imaginary part of auto/cross PSDs, i.e., those affecting the PSD matrix of modal response $\boldsymbol{H}_k$. See (4) for $\boldsymbol{Q}$ and (5) for $\boldsymbol{Q}_i$; $\boldsymbol{e}_i$ and $\boldsymbol{\Phi}$: are explained thereafter; $[\boldsymbol{Q}_i]$ denotes a block diagonal matrix containing the $\boldsymbol{Q}_i$s and $[\boldsymbol{e}_j\boldsymbol{e}_i^T]$ denotes a $m^2 \times m^2$ matrix whose (i,j)-partition is $\boldsymbol{e}_j\boldsymbol{e}_i^T$.

	$x, y = f, \zeta, \boldsymbol{S}$	S_e	$\boldsymbol{\varphi}_1, \ldots, \boldsymbol{\varphi}_m$
$x, y = f, \zeta, \boldsymbol{S}$	$J_{xy} \sim tr\Sigma[\boldsymbol{H}_k^{-1}\boldsymbol{H}_k^{(x)}\boldsymbol{H}_k^{-1}\boldsymbol{H}_k^{(y)}]$	$J_{xS_e} \sim tr[(\overline{\boldsymbol{\Phi}}^T\overline{\boldsymbol{\Phi}})^{-1}\Sigma\boldsymbol{H}_k^{-1}\boldsymbol{H}_k^{(x)}\boldsymbol{H}_k^{-1}]$	$J_{\underset{1\times mn}{x\boldsymbol{\varphi}_i}} \sim 2\boldsymbol{e}_i^T(\mathrm{Re}\Sigma\boldsymbol{H}_k^{(x)}\boldsymbol{H}_k^{-1})\boldsymbol{Q}_i$
S_e		$J_{S_eS_e} \sim N_f(n-m)S_e^{-2}$	$J_{\underset{1\times mn}{S_e\boldsymbol{\varphi}_i}} \sim 2\boldsymbol{e}_i^T(\overline{\boldsymbol{\Phi}}^T\overline{\boldsymbol{\Phi}})^{-1}(\mathrm{Re}\Sigma\boldsymbol{H}_k^{-1})\boldsymbol{Q}_i$
$\boldsymbol{\varphi}_1, \ldots, \boldsymbol{\varphi}_m$	Symmetric		$J_{\underset{mn\times mn}{\boldsymbol{\Phi}:\boldsymbol{\Phi}:}} \sim J^{(1)}_{\boldsymbol{\Phi}:\boldsymbol{\Phi}:} + J^{(2)}_{\boldsymbol{\Phi}:\boldsymbol{\Phi}:}$ $J^{(1)}_{\boldsymbol{\Phi}:\boldsymbol{\Phi}:} = 2S_e^{-1}(\mathrm{Re}\Sigma\boldsymbol{H}_k) \otimes \boldsymbol{Q}$ $J^{(2)}_{\boldsymbol{\Phi}:\boldsymbol{\Phi}:} = 2[\boldsymbol{Q}_i]^T\left\{(\mathrm{Re}\Sigma\boldsymbol{H}_k \otimes \boldsymbol{H}_k^T) + N_f[\boldsymbol{e}_j\boldsymbol{e}_i^T]\right\}[\boldsymbol{Q}_i]$

3. Bayesian OMA

The Bayesian OMA framework adopted in this work is briefly reviewed here. Consider making Bayesian inference of the properties of classically damped vibration modes based on (output-only) ambient vibration data at n DOFs of the subject structure. Without loss of generality, assume that digital acceleration data $\{\ddot{\boldsymbol{x}}_j\}_{j=0}^{N-1}$ $(n \times 1)$ is measured, from which the 'scaled' Fast Fourier Transform (FFT) can be calculated $\mathcal{F}_k = \sqrt{2\Delta t/N}\Sigma_{j=0}^{\mathcal{N}-1}\ddot{\mathbf{x}}_j e^{-2\pi \mathbf{i} jk/N}$, where Δt (sec) is the sampling interval and k is the FFT index at frequency $f_k = k/N\Delta t$ (Hz). The FFT (the sum) has been scaled by $\sqrt{2\Delta t/N}$ so that the expectation $E[\mathcal{F}_k\mathcal{F}_k^*]$ ('*' denotes complex conjugate transpose) gives the one-sided PSD matrix of data. Only the scaled FFT within a selected resonance band covering the modes of interest is used for modal ID, which is found to play a balance between ID precision (information from bands off resonance is negligible) and modelling error (ID results are immune to activities outside resonance band).

Within the resonance band the scaled FFT of data is modelled as $\mathcal{F}_k = \Sigma_{i=1}^m \boldsymbol{\varphi}_i\ddot{\eta}_{ik} + \xi_k$ where m is the number of modes; ξ_k $(n \times 1)$ is a vector of data noise, assumed to be i.i.d. among different DOFs with a common PSD S_e within the resonance band (so only band-limited white); $\boldsymbol{\varphi}_i$ $(n \times 1)$ is the mode shape, real-valued because the mode is assumed to be classically damped; $\ddot{\eta}_{ik}$ (scalar) is the scaled FFT of modal acceleration response, whose time-domain counterpart satisfies (omitting dependence on time) $\ddot{\eta}_i + 2\zeta_i\omega_i\dot{\eta}_i + \omega_i^2\eta_i = p_i$; $\omega_i = 2\pi f_i$ (rad/sec) and f_i is the natural frequency (Hz), ζ_i is the damping ratio, p_i is the modal force (per unit modal mass). Strictly speaking, the noise PSDs at different DOFs are never the same because no two data channels are identical. The BAYOMA framework so far has assumed a common noise PSD as it is found to significantly simplify mathematics, allowing development of fast algorithms for posterior statistics. Experience reveals that the ID results (both most probable value and ID uncertainty) of other modal parameters (the main interest) are insensitive to violation of this assumption unless the S/N ratio is low and the noise PSDs differ by several orders of magnitude. This is also consistent with the uncertainty law for well-separated modes where for high S/N ratios the noise PSD is asymptotically uncorrelated from the remaining parameters [23]. The modal forces $\{p_i\}_{i=1}^m$ are assumed to be stochastic stationary with a constant PSD matrix $\boldsymbol{S}$ $(m \times m$ Hermitian and positive definite) within the resonance band (so only band-limited white). The modal properties to be identified comprise $\{f_i\}_{i=1}^m$, $\{\zeta_i\}_{i=1}^m$, $\boldsymbol{S}$, S_e and $\boldsymbol{\Phi} = [\boldsymbol{\varphi}_1, \ldots, \boldsymbol{\varphi}_m]$. Accounting for its Hermitian nature,

$\boldsymbol{S}$ has m^2 parameters: m for the real diagonal entries and $m(m-1)$ for the complex-valued lower off-diagonal entries. In total there are $m+m+m^2+1+mn=(m+1)^2+mn$ parameters, subjected to m unit norm constraints on the mode shapes.

Given the scaled FFT as data, the ID results are encapsulated in the 'posterior' (i.e., given data) PDF (probability density function) of modal parameters, which is proportional to the product of the likelihood function and prior PDF. Assuming long data, the scaled FFT can be shown to follow a (circularly symmetric) complex Gaussian PDF. The likelihood function is then equal to $\exp(-L)$ where $L=nN_f\ln\pi+\Sigma\ln|\boldsymbol{E}_k|+\Sigma\boldsymbol{\mathcal{F}}_k^*\mathbf{E}_k^{-1}\boldsymbol{\mathcal{F}}_k$ is the negative log-likelihood function; $|\cdot|$ denotes the matrix determinant; the sums without index are over all k in the resonance band for modal ID (same notation throughout this work);

$$\boldsymbol{E}_k=\overline{\boldsymbol{\Phi}}\boldsymbol{H}_k\overline{\boldsymbol{\Phi}}^T+S_e\boldsymbol{I}_n \tag{1}$$

is the theoretical PSD matrix of data that depends on the modal parameters; $\boldsymbol{I}_n$ is the $n\times n$ identity matrix;

$$\overline{\boldsymbol{\Phi}}=[\overline{\boldsymbol{\varphi}}_1,\ldots,\overline{\boldsymbol{\varphi}}_m]\quad \overline{\boldsymbol{\varphi}}_i=\boldsymbol{\varphi}_i/||\boldsymbol{\varphi}_i||\quad ||\boldsymbol{\varphi}_i||^2=\boldsymbol{\varphi}_i^T\boldsymbol{\varphi}_i \tag{2}$$

is the normalised mode shape matrix; $\boldsymbol{H}_k$ is the theoretical $m\times m$ PSD matrix of modal response whose (i,j)-entry is $S_{ij}h_{ik}h_{jk}^*$ where $h_{ik}=1/[(1-\beta_{ik}^2)-\boldsymbol{i}(2\zeta_i\beta_{ik})]$ is the frequency response function between the modal force p_i and modal acceleration $\ddot{\eta}_i$; $\beta_{ik}=f_i/f_k$. Leakage has been neglected in (1) as it is asymptotically small when the data duration is long (in the sense $N_f\gg1$, see Section 4), which is assumed in the study of uncertainty laws and holds in typical cases where the ID uncertainty is under control. Empirically, a value of N_f in the order of a few tens (e.g., 30) may be considered sufficiently large for this purpose. In situations when leakage is significant there will be modelling error which is not accounted by the present study or existing uncertainty laws. See Section 10.2.6 of [18] for a discussion of this issue.

OMA data is often sufficiently long that prior information is irrelevant and hence the prior PDF is assumed to be uniform. The posterior PDF is then directly proportional to the likelihood function. It can be well-approximated by a Gaussian PDF (w.r.t. modal parameters). The mean, or equivalently 'most probable value' (MPV) of the posterior PDF maximises the likelihood function, or equivalently minimises the negative log-likelihood function. The covariance matrix of the Gaussian PDF, i.e., 'posterior covariance matrix', is equal to the inverse of the Hessian of the negative log-likelihood function at the MPV. An efficient algorithm (referred as BAYOMA) applicable for multiple (possibly close) modes has been developed which allows Bayesian OMA to be performed typically in a matter of seconds; see [22] for original work and Chapter 13 of [21] in consolidated form. See [24–27] for some recent applications.

4. Long data asymptotics

The Bayesian approach in the last section allows one to calculate the ID uncertainty of modal properties for a given data set but it does not offer any insight on how it depends on the test configuration or environment. One way to do that is to introduce a 'frequentist' assumption that the data indeed corresponds to some 'true' modal properties and study the behaviour of the posterior covariance matrix under some asymptotic yet realistic conditions such as long data and high S/N ratio. The resulting expressions are collectively referred to as 'uncertainty laws'. For globally identifiable problems such as OMA, it has been found that the asymptotic behaviour of the posterior covariance matrix is intimately related to the Fisher Information Matrix (FIM) [28]. For long data ($N_f\gg1$) the leading order of the posterior covariance matrix $\boldsymbol{C}$ is equal to the inverse of the FIM, i.e., $\boldsymbol{C}=\boldsymbol{J}^{-1}[\boldsymbol{I}+O(1/\sqrt{N_f})]$, where $\boldsymbol{I}$ denotes the identity matrix, $O(1/\sqrt{N_f})$ is the remainder that depends on data and is of the order of $1/\sqrt{N_f}$; N_f is the number of FFT points in the selected band, equal to the product of bandwidth and data duration. The matrix $\boldsymbol{J}$ is the FIM, equal to the expectation of the Hessian of negative log-likelihood function evaluated at the 'true' parameter values and assuming that the scaled FFT data is indeed distributed as the likelihood function. As the scaled FFT is complex Gaussian, it follows from a standard result in multivariate statistics [29] that the entry of FIM corresponding to generic parameters x and y is given by

$$J_{xy}=tr\Sigma[\boldsymbol{E}_k^{-1}\boldsymbol{E}_k^{(x)}\boldsymbol{E}_k^{-1}\boldsymbol{E}_k^{(y)}] \tag{3}$$

where $tr(\cdot)$ denotes the trace of a square matrix, i.e., sum of diagonal entries; the superscript '(x)' denotes a derivative w.r.t. x. On the other hand, it should be noted that, with some abuse of notation, in the FIM, the parameter symbols in the expression represent the 'true' value of properties rather than the dummy variable in Bayesian inference. That is, the FIM is a function of the true parameter values and not the data (which has already been averaged in the expectation).

It should be noted that the ID uncertainty in this work (as in BAYOMA) refers to that implied by the posterior PDF of modal parameters in a Bayesian context. The connection with frequentist concept lies only in the additional assumption that the data indeed follows a distribution for some 'true values' of modal parameters. This assumption is introduced only for the study of uncertainty laws (to understand uncertainty). It is not involved in the modal identification process where uncertainty for a given data set is calculated (but whose value provides no understanding). Detailed discussion of the meaning and interpretation of uncertainty in Bayesian and frequentist sense can be found in [28] and Section 9.6 of [21].

5. Key theoretical findings

Developing insights into ID uncertainty requires analytical investigation of FIM and its inverse to give the asymptotic posterior covariance matrix as the uncertainty law, if possible, in the form of explicit closed form expressions that link with test configuration and environment. This has been accomplished for well-separated modes but turns out to be very challenging for close modes. As the first key contribution of this work, we obtained asymptotic expressions for the FIM for high S/N ratio ($S_e \to 0$). The results are summarised in Table 2. When $m = 1$, it gives the same expressions for well-separated modes that have been previously obtained; see Table 16.1 in Section 16.1.1 of [21]. In Table 2,

$$\boldsymbol{Q} = \boldsymbol{I}_n - \overline{\boldsymbol{\Phi}}(\overline{\boldsymbol{\Phi}}^T\overline{\boldsymbol{\Phi}})^{-1}\overline{\boldsymbol{\Phi}}^T \tag{4}$$

$$\underset{m\times n}{\boldsymbol{Q}_i} = (\overline{\boldsymbol{\Phi}}^T\overline{\boldsymbol{\Phi}})^{-1}\overline{\boldsymbol{\Phi}}^T(\boldsymbol{I}_n - \overline{\boldsymbol{\varphi}}_i\overline{\boldsymbol{\varphi}}_i^T) \qquad \underset{m^2\times mn}{[\boldsymbol{Q}_i]} = \begin{bmatrix} \boldsymbol{Q}_1 & & \\ & \ddots & \\ & & \boldsymbol{Q}_m \end{bmatrix} \tag{5}$$

$\boldsymbol{e}_i$ is a $m \times 1$ zero vector except for the ith entry equal to 1; $[\boldsymbol{e}_j\boldsymbol{e}_i^T]$ denotes a $m^2 \times m^2$ matrix whose (i,j)-partition is $\boldsymbol{e}_j\boldsymbol{e}_i^T$; $\boldsymbol{\Phi}_{:}$ is the 'vectorisation' of $\boldsymbol{\Phi}$, i.e., a $mn \times 1$ vector obtained by stacking the columns of $\boldsymbol{\Phi}$ column-wise. In the derivation, it has been assumed that the mode shapes are linearly independent (but not necessarily orthogonal) and modal forces are not perfectly coherent (i.e., $\boldsymbol{S}$ non-singular), for otherwise the modal ID problem degenerates. The derivation will be outlined in Section 6 with details postponed to Appendix A for J_{xy} $(x, y = \{f, \zeta, \boldsymbol{S}\})$, J_{xS_e} and $J_{S_eS_e}$; and to Appendices B and C for $J_{x\boldsymbol{\varphi}_i}$, $J_{S_e\boldsymbol{\varphi}_i}$ and $J_{\boldsymbol{\Phi}_{:}\boldsymbol{\Phi}_{:}}$. Their asymptotic correctness will be verified in Section 10.1.

As the second (but no less important) key contribution of this work, based on Table 2, we investigate analytically the eigenvalue properties of $\boldsymbol{J}_{\boldsymbol{\Phi}_{:}\boldsymbol{\Phi}_{:}}$, the full FIM $\boldsymbol{J}$ (i.e., comprising all parameters) and hence the high S/N asymptotic posterior covariance matrix. We found that the eigenvectors of the full FIM, and hence the asymptotic covariance matrix, comprise three types induced by those of $\boldsymbol{J}_{\boldsymbol{\Phi}_{:}\boldsymbol{\Phi}_{:}}$ that carry independent and distinctive influence on ID uncertainty. They are summarised in Table 3; the definitions of $\mathcal{N}$, $\mathcal{M}$ and $\mathcal{M}_\perp$ in the table will become apparent in Section 7. Theoretical details can be found in Section 8. The theoretical findings will be illustrated in Section 10 using synthetic and field data.

As a remark, for well-separated modes a fundamental definition of S/N ratio that directly affects ID uncertainty is the PSD ratio of modal response to noise at the natural frequency [23]. In this case high S/N ratio refers to the case when this ratio is large compared to 1. For close modes the present work has not yet concluded a fundamental definition for S/N ratio with the same success mentioned above. The condition $S_e \to 0$ was given earlier as a simple limit condition to qualify for the theoretical results. See also (47) that is a dimensionless but more involved condition that can potentially lead to a definition in the future useful for quantifying ID uncertainty for close modes. When applying the asymptotic results for cases with clearly different channel noise PSDs, one may use a value of S_e with a representative order of magnitude, e.g., the geometric mean of channel noise PSDs.

Table 3
Eigenvalue properties of full FIM $\boldsymbol{J}$; MSS = mode shape subspace; assume mode shapes $\{\boldsymbol{\varphi}_1, ..., \boldsymbol{\varphi}_m\}$ appear in the last mn entries of the full set of modal parameters; see Table 4 for definitions of $\mathcal{N}$, $\mathcal{M}$ and $\mathcal{M}_\perp$.

Type	Eigenvalues	Eigenvectors	Remark
0	m zero eigenvalues	Of the form $[\boldsymbol{0};\boldsymbol{b}]$ where $\boldsymbol{b}$ is in $\mathcal{N}$ and is given by $\begin{bmatrix}\boldsymbol{\varphi}_1\\ \end{bmatrix}, \begin{bmatrix}\boldsymbol{\varphi}_2\\ \end{bmatrix}, ..., \begin{bmatrix}\\ \boldsymbol{\varphi}_m\end{bmatrix}$	– arise from norm constraints on mode shapes; – carry no ID uncertainty
1	$m(n-m)$ eigenvalues, equal to λ_i (multiplicity $n-m$), $i = 1, ..., m$	Of the form $[\boldsymbol{0};\boldsymbol{b}]$ where $\boldsymbol{b}$ is in $\mathcal{M}_\perp$ and is given by $\boldsymbol{a}_i \otimes \boldsymbol{b}_j$, $i = 1, ..., m$; $j = 1, ..., n-m$; $\{\boldsymbol{a}_i\}_{i=1}^m$ are eigenvectors of $2S_e^{-1}\mathrm{Re}\boldsymbol{\Sigma}\boldsymbol{H}_k$ with eigenvalues $\{\lambda_i\}_{i=1}^m$; $\{\boldsymbol{b}_j\}_{j=1}^{n-m}$ are the $(n-m)$ eigenvectors of $\boldsymbol{Q}$ with eigenvalue 1	– induce ID uncertainty of mode shape perpendicular to MSS – induce no ID uncertainty in other parameters – found previously in single mode – induced uncertainty vanishes for noiseless data, negligible for high S/N ratio
2	$(m+1)^2 + m(m-1)$ eigenvalues, equal to those of the eigenvalue problem $\boldsymbol{J}_c\boldsymbol{x} = \lambda\boldsymbol{B}\boldsymbol{x}$ in (25)	Of the form $\boldsymbol{\theta} = [\boldsymbol{a};\boldsymbol{b}]$, where $\boldsymbol{b} = \mathbf{U}\boldsymbol{\alpha}$ is in $\mathcal{M}$; $\boldsymbol{U}$ contains a basis for $\mathcal{M}$; $\boldsymbol{x} = [\mathbf{a};\boldsymbol{\alpha}]$ is eigenvector of the eigenvalue problem $\boldsymbol{J}_c\boldsymbol{x} = \lambda\boldsymbol{B}\boldsymbol{x}$ in (25)	– induce ID uncertainty of mode shape within MSS; – correlated with ID uncertainty of other parameters; – not found in single mode, new discovery unique to close modes; – induced uncertainty does not vanish for noiseless data, can be significant regardless of S/N ratio

6. Outline of derivations

The FIM in (3) is a generic expression that does not tell how it depends on modal properties, which can be very complicated in general situations. In this section we outline the derivation of the explicit expressions for the FIM in Table 2, which are asymptotically correct for high S/N ratio, i.e., as the noise PSD $S_e \to 0$. The first step is to approximate the inverse of $\boldsymbol{E}_k = \overline{\boldsymbol{\Phi}}\boldsymbol{H}_k\overline{\boldsymbol{\Phi}}^T + S_e\boldsymbol{I}_n$ in (1) by a Taylor expansion for small S_e. For this purpose, one should not take $\boldsymbol{E}_k \sim \overline{\boldsymbol{\Phi}}\boldsymbol{H}_k\overline{\boldsymbol{\Phi}}^T$ because $\overline{\boldsymbol{\Phi}}\boldsymbol{H}_k\overline{\boldsymbol{\Phi}}^T$ is rank deficient. One proper way is to use the matrix inverse lemma [30,31] to obtain

$$\boldsymbol{E}_k^{-1} = S_e^{-1}(\boldsymbol{I}_n - \overline{\boldsymbol{\Phi}}\boldsymbol{P}_k^{-1}\overline{\boldsymbol{\Phi}}^T) \tag{6}$$

where

$$\boldsymbol{P}_k = \overline{\boldsymbol{\Phi}}^T\overline{\boldsymbol{\Phi}} + S_e\boldsymbol{H}_k^{-1} \tag{7}$$

Assuming $n \geq m$ and the columns of $\overline{\boldsymbol{\Phi}}$ are linearly independent, $\overline{\boldsymbol{\Phi}}^T\overline{\boldsymbol{\Phi}}$ $(m \times m)$ has full rank and so $\boldsymbol{P}_k \sim \overline{\boldsymbol{\Phi}}^T\overline{\boldsymbol{\Phi}}$ is a legitimate 0th order approximation. However, it turns out that this does not give the correct approximation for $\boldsymbol{E}_k^{-1}$ w.r.t. parameters affecting $\boldsymbol{H}_k$. Up to second order,

$$\boldsymbol{P}_k^{-1} \sim (\overline{\boldsymbol{\Phi}}^T\overline{\boldsymbol{\Phi}})^{-1}\left[\overline{\boldsymbol{\Phi}}^T\overline{\boldsymbol{\Phi}} - \boldsymbol{\varepsilon}_k + \boldsymbol{\varepsilon}_k(\overline{\boldsymbol{\Phi}}^T\overline{\boldsymbol{\Phi}})^{-1}\boldsymbol{\varepsilon}_k\right](\overline{\boldsymbol{\Phi}}^T\overline{\boldsymbol{\Phi}})^{-1} \qquad \boldsymbol{\varepsilon}_k = S_e\boldsymbol{H}_k^{-1} \tag{8}$$

Substituting into (6) gives

$$\boldsymbol{E}_k^{-1} \sim \underbrace{S_e^{-1}\boldsymbol{Q}}_{\text{0th order}} + \underbrace{S_e^{-1}\boldsymbol{R}^T\boldsymbol{\varepsilon}_k\boldsymbol{R}}_{\text{1st order}} - \underbrace{S_e^{-1}\boldsymbol{R}^T\boldsymbol{\varepsilon}_k(\overline{\boldsymbol{\Phi}}^T\overline{\boldsymbol{\Phi}})^{-1}\boldsymbol{\varepsilon}_k\boldsymbol{R}}_{\text{2nd order}} \tag{9}$$

where $\boldsymbol{Q} = \boldsymbol{I}_n - \overline{\boldsymbol{\Phi}}(\overline{\boldsymbol{\Phi}}^T\overline{\boldsymbol{\Phi}})^{-1}\overline{\boldsymbol{\Phi}}^T$ was defined in (4); and

$$\boldsymbol{R} = (\overline{\boldsymbol{\Phi}}^T\overline{\boldsymbol{\Phi}})^{-1}\overline{\boldsymbol{\Phi}}^T \tag{10}$$

The matrices $\boldsymbol{Q}$ and $\boldsymbol{R}$ appear frequently in the derivation and their properties are worth-noting. First, $\boldsymbol{R}\overline{\boldsymbol{\Phi}} = \boldsymbol{I}_m$ and $\boldsymbol{R}\boldsymbol{u} = \boldsymbol{0}$ for any $\boldsymbol{u}$ orthogonal to the 'mode shape subspace' (MSS), i.e., space spanned by mode shapes $\{\overline{\boldsymbol{\varphi}}_i\}_{i=1}^m$. The matrix $\boldsymbol{Q}$ is a zero mapping in the MSS and an identity mapping in the orthogonal complement of MSS. The zero mapping can be seen from $\boldsymbol{Q}\overline{\boldsymbol{\Phi}} = \boldsymbol{0}$. The identity mapping can be seen from $\overline{\boldsymbol{\Phi}}^T\boldsymbol{u} = \boldsymbol{0}$ for any $\boldsymbol{u}$ orthogonal to MSS. These properties imply that $\boldsymbol{Q}$ has m zero eigenvalues with an orthogonal basis of eigenvectors in the MSS. The remaining $n - m$ eigenvalues are all equal to 1 with an orthogonal basis of eigenvectors in the orthogonal complement of the MSS.

The derivatives in (3) w.r.t. different groups of parameters are given by

$$\boldsymbol{E}_k^{(x)} = \overline{\boldsymbol{\Phi}}\boldsymbol{H}_k^{(x)}\overline{\boldsymbol{\Phi}}^T \qquad (x = f, \zeta, \boldsymbol{S}) \qquad\qquad \boldsymbol{E}_k^{(S_e)} = \boldsymbol{I}_n \tag{11}$$

$$\boldsymbol{E}_k^{(\Phi_{ri})} = \overline{\boldsymbol{\Phi}}^{(\Phi_{ri})}\boldsymbol{H}_k\overline{\boldsymbol{\Phi}}^T + \overline{\boldsymbol{\Phi}}\boldsymbol{H}_k\overline{\boldsymbol{\Phi}}^{(\Phi_{ri})} \tag{12}$$

where Φ_{ri} denotes the (r,i)-entry of $\boldsymbol{\Phi}$. Using (9) and (11), considering the leading order terms and simplifying gives J_{xy}, J_{xS_e} and $J_{S_eS_e}$ in Table 2 $(x, y = \{f, \zeta, \boldsymbol{S}\})$. Details can be found in Appendix A. For the entries in FIM related to mode shapes, using (12), considering the leading order terms and simplifying gives (see Appendix B for details):

$$J_{x\Phi_{ri}} \sim 2\text{Re}tr\Sigma\left[\boldsymbol{H}_k^{(x)}\boldsymbol{H}_k^{-1}\boldsymbol{R}\overline{\boldsymbol{\Phi}}^{(\Phi_{ri})}\right] \qquad x = f, \zeta, \boldsymbol{S} \tag{13}$$

$$J_{S_e\Phi_{ri}} \sim 2\text{Re}tr\Sigma\left[(\overline{\boldsymbol{\Phi}}^T\overline{\boldsymbol{\Phi}})^{-1}\boldsymbol{H}_k^{-1}\boldsymbol{R}\overline{\boldsymbol{\Phi}}^{(\Phi_{ri})}\right] \tag{14}$$

$$J_{xy} \sim J_{xy}^{(1)} + J_{xy}^{(2)} \qquad x, y = \boldsymbol{\Phi} \tag{15}$$

where '$x, y = \boldsymbol{\Phi}$' denotes that x and y are entries in $\boldsymbol{\Phi}$; and

$$J_{xy}^{(1)} = 2S_e^{-1}tr\left[\boldsymbol{Q}\overline{\boldsymbol{\Phi}}^{(x)}(\text{Re}\Sigma\boldsymbol{H}_k)\overline{\boldsymbol{\Phi}}^{(y)T}\right] \qquad x, y = \boldsymbol{\Phi} \tag{16}$$

$$J_{xy}^{(2)} = 2N_ftr\left[\boldsymbol{R}\overline{\boldsymbol{\Phi}}^{(x)}\boldsymbol{R}\overline{\boldsymbol{\Phi}}^{(y)}\right] + 2\text{Re}tr\Sigma\left[\boldsymbol{R}^T\boldsymbol{H}_k^{-1}\boldsymbol{R}\overline{\boldsymbol{\Phi}}^{(x)}\boldsymbol{H}_k\overline{\boldsymbol{\Phi}}^{(y)T}\right] \qquad x, y = \boldsymbol{\Phi} \tag{17}$$

To express in more explicit form, the derivative $\overline{\boldsymbol{\Phi}}^{(\Phi_{ri})}$ from (61) in Appendix I of [22] is used:

$$\overline{\boldsymbol{\Phi}}^{(\Phi_{ri})} = \left[\overline{\boldsymbol{\varphi}}_1^{(\Phi_{ri})} \quad \cdots \quad \overline{\boldsymbol{\varphi}}_m^{(\Phi_{ri})} \right] = \| \boldsymbol{\varphi}_i \|^{-1} (\boldsymbol{I}_n - \overline{\boldsymbol{\varphi}}_i \overline{\boldsymbol{\varphi}}_i^T) \boldsymbol{e}_r \boldsymbol{e}_i^T \tag{18}$$

Substituting (18) into (13)–(17), considering the leading order term, simplifying and assemblying in matrix form gives the final expressions of $J_{x\varphi_i}$, $J_{S_e\varphi_i}$ and $J_{\Phi:\Phi:}$ in Table 2. See Appendix C for details.

7. Principal subspaces of mode shape uncertainty

The eigenvalue properties of the high S/N asymptotic FIM in Table 2 will be investigated analytically in Section 8. For this purpose, some important concepts are reviewed/introduced in this section. The mode shape $\boldsymbol{\varphi}_i$ of a particular mode i is an $n \times 1$ vector in the n-dimensional Euclidean space, denoted by R^n. The mode shape subspace (MSS), denoted by M, is the subspace in R^n spanned by $\{\boldsymbol{\varphi}_1, ..., \boldsymbol{\varphi}_m\}$, i.e., the collection of all vectors of the form $\boldsymbol{x} = \Sigma_{i=1}^m a_i \boldsymbol{\varphi}_i$ where $\{a_i\}_{i=1}^m$ are real numbers. The orthogonal complement of M, denoted by $M_\perp$, is the subspace in R^n comprising all vectors orthogonal to those in M, i.e., the collection of all vectors $\boldsymbol{y}$ such that $\boldsymbol{y}^T\boldsymbol{x} = 0$ for any $\boldsymbol{x}$ in M. Assuming $\{\boldsymbol{\varphi}_1, ..., \boldsymbol{\varphi}_m\}$ are linearly independent, M has dimension m and $M_\perp$ has dimension $n - m$. Symbolically this can be written as $R^n = M + M_\perp$. The same is also true for their dimensions, i.e., $n = m + (n - m)$. For a given i, let $\{\boldsymbol{u}_{ij}\}_{j=1}^{m-1}$ be a basis in the orthogonal complement of $\boldsymbol{\varphi}_i$ in M. That is, $\boldsymbol{\varphi}_i$ and $\{\boldsymbol{u}_{ij}\}_{j=1}^{m-1}$ form a basis in M but $\boldsymbol{\varphi}_i$ is orthogonal to $\boldsymbol{u}_{ij}$. Let also $\{\boldsymbol{v}_{ij}\}_{j=1}^{n-m}$ be a basis in $M_\perp$. Then $\boldsymbol{\varphi}_i$, $\{\boldsymbol{u}_{ij}\}_{j=1}^{m-1}$ and $\{\boldsymbol{v}_{ij}\}_{j=1}^{n-m}$ together form a basis in R^n.

As a note, $\{\boldsymbol{u}_{ij}\}_{j=1}^{m-1}$ are linearly independent but need not be orthogonal. One geometrically intuitive possibility is for $\boldsymbol{u}_{ij}$ to be a vector along the tangential direction from $\boldsymbol{\varphi}_i$ that rotates from $\boldsymbol{\varphi}_i$ towards $\boldsymbol{\varphi}_j$ in the hyperplane formed by them:

$$\boldsymbol{u}_{ij} = \boldsymbol{\varphi}_j - \boldsymbol{\varphi}_i r_{ij} \quad r_{ij} = \frac{\boldsymbol{\varphi}_i^T \boldsymbol{\varphi}_j}{\boldsymbol{\varphi}_i^T \boldsymbol{\varphi}_i} \quad j \neq i \tag{19}$$

As a check, $\boldsymbol{u}_{ij}$ lies in the plane formed by $\boldsymbol{\varphi}_i$ and $\boldsymbol{\varphi}_j$; and $\boldsymbol{\varphi}_i^T \boldsymbol{u}_{ij} = 0$. Another possibility is for $\{\boldsymbol{u}_{ij}\}_{j=1}^{m-1}$ to be a set of orthogonal basis from the Gram-Schmidt procedure [30]. The choice of $\{\boldsymbol{u}_{ij}\}_{j=1}^{m-1}$ is discussed here for concreteness only. It does not affect the theory developed.

The $n \times n$ posterior covariance matrix of $\boldsymbol{\varphi}_i$ only informs the uncertainty of $\boldsymbol{\varphi}_i$ but not its correlation with other mode shapes. A complete description of the uncertainty with m modes requires one to study the $mn \times mn$ posterior covariance matrix of the $mn \times 1$ vector $\boldsymbol{\Phi} := [\boldsymbol{\varphi}_1; ...; \boldsymbol{\varphi}_m]$, (';' denotes stacking column-wise). Although it may appear artificial at this stage, it is useful to introduce three orthogonally complementary spaces in R^{mn}, namely, $\mathcal{N}$, $\mathcal{M}$ and $\mathcal{M}_\perp$, which are induced by $\boldsymbol{\varphi}_i$, $\boldsymbol{u}_{ij}$ and $\boldsymbol{v}_{ij}$, respectively. They are defined in the first three columns of Table 4; the remaining columns will become apparent in Section 8. Symbolically, $R^{mn} = \mathcal{N} + \mathcal{M} + \mathcal{M}_\perp$. In the basis vector for $\mathcal{N}$, the Kronecker product $\boldsymbol{e}_i \otimes \boldsymbol{\varphi}_i$ ($mn \times 1$) puts $\boldsymbol{\varphi}_i$ in the ith partition and the remaining $(m - 1)$ partitions (each $n \times 1$) are all zero. Similarly, the basis vectors $\boldsymbol{e}_i \otimes \boldsymbol{u}_{ij}$ (for $\mathcal{M}$) and $\boldsymbol{e}_i \otimes \boldsymbol{v}_{ij}$ (for $\mathcal{M}_\perp$) have their ith partition equal to $\boldsymbol{u}_{ij}$ and $\boldsymbol{v}_{ij}$, respectively; and the remaining partitions are zero. Fig. 3 illustrates the three subspaces. As we will see in Section 8, $\mathcal{N}$ is associated with mode shape norm constraint and carries no uncertainty; $\mathcal{M}$ is associated with mode shape uncertainty within the MSS; $\mathcal{M}_\perp$ is associated with uncertainty orthogonal to the MSS.

8. Eigenvalue properties

In the derivation of uncertainty laws the mode shapes always present the major hurdle because of their dimension growing with the number of DOFs. For well-separated modes this has been resolved by discovering that the mode shape is asymptotically uncorrelated from the remaining parameters. Numerical experiments reveal that this is not the case for close modes and the correlation structure is non-trivial. In this section we analyse analytically, in turn, the eigenvalue properties of $\boldsymbol{J}_{\Phi:\Phi:}^{(1)}$,

Table 4
Principal subspaces of mode shape uncertainty in R^{mn}; MSS = mode shape subspace.

Subspace	Dimension	Basis	$J_{\Phi:\Phi:}^{(1)}$	$J_{\Phi:\Phi:}^{(2)}$	$J_{\Phi:\Phi:}$	Remark
$\mathcal{N}$	m	$\boldsymbol{e}_i \otimes \boldsymbol{\varphi}_i$ $i = 1, ..., m$	Null space	Null space	Null space	Norm-constrained subspace
$\mathcal{M}$	$m(m-1)$	$\boldsymbol{e}_i \otimes \boldsymbol{u}_{ij}$ $i = 1, ..., m$ $j = 1, ..., m-1$	Null space	Non-zero eigenvalues, non-trivial	Eigenvalues and eigenvectors equal to those of $J_{\Phi:\Phi:}^{(2)}$ in this space	Subspace containing all possible mode shape deviations within MSS
$\mathcal{M}_\perp$	$m(n-m)$	$\boldsymbol{e}_i \otimes \boldsymbol{v}_{ij}$ $i = 1, ..., m$ $j = 1, ..., n-m$	Eigenvalues equal to those of $2S_e^{-1}\mathrm{Re}\Sigma\boldsymbol{H}_k$, each with multiplicity $n - m$	Null space	Eigenvalues and eigenvectors equal to those of $J_{\Phi:\Phi:}^{(1)}$ in this space	Subspace containing all possible mode shape deviations orthogonal to MSS

	$\mathcal{N}$ Dim. m	$\mathcal{M}$ Dim. m(m-1)	$\mathcal{M}_\perp$ Dim. m(n-m)
m = 1 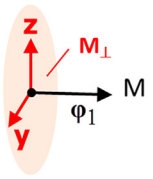	Dim. = 1 φ_1	Dim. = 0 Null	Dim. = 2 **z, y**
m = 2 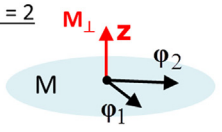	Dim. = 2 $\begin{bmatrix}\varphi_1\\0\end{bmatrix},\begin{bmatrix}0\\\varphi_2\end{bmatrix}$	Dim. = 2 $\begin{bmatrix}\varphi_2-\varphi_1 r_{12}\\0\end{bmatrix},\begin{bmatrix}0\\\varphi_1-\varphi_2 r_{21}\end{bmatrix}$	Dim. = 2 $\begin{bmatrix}\mathbf{z}\\0\end{bmatrix},\begin{bmatrix}0\\\mathbf{z}\end{bmatrix}$
m = 3 $M_\perp$ is null 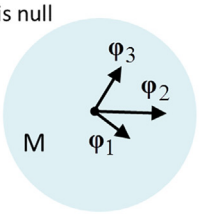	Dim. = 3 $\begin{bmatrix}\varphi_1\\0\\0\end{bmatrix},\begin{bmatrix}0\\\varphi_2\\0\end{bmatrix},\begin{bmatrix}0\\0\\\varphi_3\end{bmatrix}$	Dim. = 6 $\begin{bmatrix}\varphi_2-\varphi_1 r_{12}\\0\\0\end{bmatrix},\begin{bmatrix}\varphi_3-\varphi_1 r_{13}\\0\\0\end{bmatrix}$ $\begin{bmatrix}0\\\varphi_1-\varphi_2 r_{21}\\0\end{bmatrix},\begin{bmatrix}0\\\varphi_3-\varphi_2 r_{23}\\0\end{bmatrix}$ $\begin{bmatrix}0\\0\\\varphi_1-\varphi_3 r_{31}\end{bmatrix},\begin{bmatrix}0\\0\\\varphi_2-\varphi_3 r_{32}\end{bmatrix}$	Dim. = 0 Null

Fig. 3. Example of basis for $\mathcal{N}$, $\mathcal{M}$ and $\mathcal{M}_\perp$ for $n = 3$ measured DOFs and different number of modes m. When $m = 1$, M (mode shape subspace) is the line along $\boldsymbol{\varphi}_1$; when $m = 2$, M is the 2-D plane spanned by $\boldsymbol{\varphi}_1$ and $\boldsymbol{\varphi}_2$; when $m = 3$, M is the whole 3-D space; $r_{ij} = (\boldsymbol{\varphi}_i^T\boldsymbol{\varphi}_j)/(\boldsymbol{\varphi}_i^T\boldsymbol{\varphi}_i)$.

$\boldsymbol{J}^{(2)}_{\boldsymbol{\Phi}:\boldsymbol{\Phi}:}, \boldsymbol{J}_{\boldsymbol{\Phi}:\boldsymbol{\Phi}:}$ and the full FIM $\boldsymbol{J}$ in Table 2; and finally the high S/N asymptotic posterior covariance matrix $\boldsymbol{C} = \boldsymbol{J}^{-1}$. This allows us to understand the principal directions in which the ID uncertainty of modal parameters, especially the mode shapes, takes place. As we will see, the results are remarkably definitive and characteristic, despite complexity of the close modes problem and the mathematics involved.

8.1. $\boldsymbol{J}^{(1)}_{\boldsymbol{\Phi}:\boldsymbol{\Phi}:}$ (Type 1)

The eigenvalue properties of $\boldsymbol{J}^{(1)}_{\boldsymbol{\Phi}:\boldsymbol{\Phi}:}$ follow directly from the standard result in linear algebra that if A $(m \times m)$ has eigenvalue a_i with eigenvector u_i $(i = 1, \ldots, m)$ and B $(n \times n)$ has eigenvalue b_j with eigenvector v_j $(j = 1, \ldots, n)$ then the Kronecker product $A \otimes B$ has eigenvalue $a_i b_j$ with eigenvector $u_i \otimes v_j$ $(i = 1, \ldots, m; j = 1, \ldots, n)$. Applying this result, the eigenvalues of $J^{(1)}_{\boldsymbol{\Phi}:\boldsymbol{\Phi}:}$ are the product of those of $2S_e^{-1}\mathrm{Re}\boldsymbol{\Sigma}\boldsymbol{H}_k$ and $\boldsymbol{Q}$. The eigenvectors are the Kronecker product of the eigenvectors of $2S_e^{-1}\mathrm{Re}\boldsymbol{\Sigma}\boldsymbol{H}_k$ and $\boldsymbol{Q}$. Since $\boldsymbol{Q}$ has m zero eigenvalues with eigenvectors $\{\boldsymbol{\varphi}_1, \ldots, \boldsymbol{\varphi}_m\}$, $J^{(1)}_{\boldsymbol{\Phi}:\boldsymbol{\Phi}:}$ has m^2 zero eigenvalues. The basis vectors $\{\boldsymbol{e}_i \otimes \boldsymbol{\varphi}_i\}_{i=1}^m$ of $\mathcal{N}$ are among the eigenvectors with zero eigenvalue, which can be verified by direct substitution and noting that $\boldsymbol{Q}_i\boldsymbol{\varphi}_i = \boldsymbol{0}$. In general, for the zero eigenvalues, resulting from Kronecker product the ith partition of the eigenvector is a multiple of $\boldsymbol{\varphi}_i$ and hence lies in the MSS. Since a linear combination of eigenvectors of the same eigenvalue is also an eigenvector, in the context of Table 4 the zero eigenvalue can be considered to have m eigenvectors in $\mathcal{N}$ and $m(m-1)$ eigenvectors in $\mathcal{M}$.

Other than the zero eigenvalue, the remaining $(n-m)$ eigenvalues of $\boldsymbol{Q}$ are all equal to 1 with eigenvectors in $M_\perp$. The remaining $m(n-m)$ eigenvalues of $J^{(1)}_{\boldsymbol{\Phi}:\boldsymbol{\Phi}:}$ are then equal to the m eigenvalues of $2S_e^{-1}\mathrm{Re}\boldsymbol{\Sigma}\boldsymbol{H}_k$, each with multiplicity (i.e., repeating) $n-m$. The eigenvectors of this type lie in the orthogonal complement of $\mathcal{N}$ and $\mathcal{M}$, i.e., $\mathcal{M}_\perp$. These results are summarised in the fourth column of Table 4.

8.2. $\boldsymbol{J}^{(2)}_{\boldsymbol{\Phi}:\boldsymbol{\Phi}:}$ (Type 2)

The eigenvalue properties of $J^{(2)}_{\boldsymbol{\Phi}:\boldsymbol{\Phi}:}$ are complementary to $J^{(1)}_{\boldsymbol{\Phi}:\boldsymbol{\Phi}:}$. The $m(n-m)$ eigenvectors of $J^{(1)}_{\boldsymbol{\Phi}:\boldsymbol{\Phi}:}$ with non-zero eigenvalue (hence in $\mathcal{M}_\perp$) are eigenvectors of $J^{(2)}_{\boldsymbol{\Phi}:\boldsymbol{\Phi}:}$ with zero eigenvalue. To see this, such an eigenvector is of the form $\boldsymbol{v} = [a_1\boldsymbol{u}; \cdots; a_m\boldsymbol{u}]$ (';' denotes stacking column-wise), where $[a_1, \ldots, a_m]^T$ is an eigenvector of $2S_e^{-1}\mathrm{Re}\boldsymbol{\Sigma}\boldsymbol{H}_k$ and $\boldsymbol{u}$ is an eigenvector of $\boldsymbol{Q}$ with eigenvalue 1, i.e., in $M_\perp$. Then $\overline{\boldsymbol{\Phi}}^T\boldsymbol{u} = \boldsymbol{0}$ and $\overline{\boldsymbol{\varphi}}_i^T\boldsymbol{u} = 0$, and from (5) we can deduce $\boldsymbol{Q}_i\boldsymbol{u} = \boldsymbol{0}$. This implies that

$$\begin{bmatrix} \boldsymbol{Q}_1 & & \\ & \ddots & \\ & & \boldsymbol{Q}_m \end{bmatrix} \begin{bmatrix} a_1\boldsymbol{u} \\ \vdots \\ a_m\boldsymbol{u} \end{bmatrix} = \begin{bmatrix} a_1\boldsymbol{Q}_1\boldsymbol{u} & & \\ & \ddots & \\ & & a_m\boldsymbol{Q}_m\boldsymbol{u} \end{bmatrix} = \boldsymbol{0} \tag{20}$$

and so from the expression of $J^{(2)}_{\Phi:\Phi:}$ in Table 2 we can deduce $J^{(2)}_{\Phi:\Phi:}\boldsymbol{u} = \boldsymbol{0}$. By a similar argument, the vectors in $\mathcal{N}$ are also null vectors of $J^{(2)}_{\Phi:\Phi:}$. Consequently, $J^{(2)}_{\Phi:\Phi:}$ only has $mn - m(n-m) - m = m(m-1)$ possibly non-zero eigenvalues whose eigenvectors lie in the orthogonal complement of both $\mathcal{N}$ and $\mathcal{M}_\perp$, i.e., $\mathcal{M}$. These results are summarised in the fifth column of Table 4.

8.3. Mode shape FIM $\boldsymbol{J}_{\Phi:\Phi:}$

The eigenvalue properties of $J_{\Phi:\Phi:}$ inherit directly from those of $J^{(1)}_{\Phi:\Phi:}$ and $J^{(2)}_{\Phi:\Phi:}$. The null space $\mathcal{N}$ is common to $J^{(1)}_{\Phi:\Phi:}$ and $J^{(2)}_{\Phi:\Phi:}$ and is therefore also a null space for $J_{\Phi:\Phi:}$. In $\mathcal{M}$ where $J^{(1)}_{\Phi:\Phi:}$ is a zero mapping, the eigenvalues and eigenvectors of $J_{\Phi:\Phi:}$ directly inherit from those of $J^{(2)}_{\Phi:\Phi:}$. To see this, if $\boldsymbol{u}$ in $\mathcal{M}$ is an eigenvector of $J^{(2)}_{\Phi:\Phi:}$ with eigenvalue λ, then $J^{(1)}_{\Phi:\Phi:}\boldsymbol{u} = \boldsymbol{0}$ and $J^{(2)}_{\Phi:\Phi:}\boldsymbol{u} = \lambda\boldsymbol{u}$, and so $J_{\Phi:\Phi:}\boldsymbol{u} = J^{(1)}_{\Phi:\Phi:}\boldsymbol{u} + J^{(2)}_{\Phi:\Phi:}\boldsymbol{u} = \lambda\boldsymbol{u}$, i.e., $\boldsymbol{u}$ is also an eigenvector of $J_{\Phi:\Phi:}$ with the same eigenvalue λ. By the same argument, in $\mathcal{M}_\perp$ where $J^{(2)}_{\Phi:\Phi:}$ is a zero mapping, the eigenvalues and eigenvectors of $J_{\Phi:\Phi:}$ inherit directly from those of $J^{(1)}_{\Phi:\Phi:}$. These are summarised in the sixth column of Table 4.

8.4. Full FIM $\boldsymbol{J}$

The eigenvalue properties of the full FIM $\boldsymbol{J}$ can be reasoned from those of $J_{\Phi:\Phi:}$. Let ϖ be a vector containing all parameters other than mode shapes so that $\boldsymbol{\theta} = [\varpi; \boldsymbol{\Phi}:]$ contains all modal parameters and $\boldsymbol{J}$ is the full FIM w.r.t. $\boldsymbol{\theta}$. Let $\boldsymbol{v} = [\boldsymbol{v}_1; \ldots; \boldsymbol{v}_m]$ be an eigenvector of $J_{\Phi:\Phi:}$ with eigenvalue λ and it lies either in $\mathcal{N}$ (dim. m, Type 0) or $\mathcal{M}_\perp$ (dim. $m(n-m)$, Type 1). When $\boldsymbol{v}$ is in $\mathcal{N}$, $\boldsymbol{v}_i \propto \boldsymbol{\varphi}_i$; when $\boldsymbol{v}$ is in $\mathcal{M}_\perp$, $\boldsymbol{v}_i$ is in $\mathcal{M}_\perp$. In either case $\boldsymbol{Q}_i\boldsymbol{v}_i = \boldsymbol{0}$. For all remaining parameters x from ϖ, $J_{x\boldsymbol{\varphi}_i}$ has $\boldsymbol{Q}_i$ on its right end (see Table 2) and so $J_{x\boldsymbol{\Phi}:}\boldsymbol{v} = [J_{x\boldsymbol{\varphi}_1}\boldsymbol{v}_1, \ldots, J_{x\boldsymbol{\varphi}_m}\boldsymbol{v}_m] = \boldsymbol{0}$. Then

$$\boldsymbol{J}\begin{bmatrix} \boldsymbol{0} \\ \boldsymbol{v} \end{bmatrix} = \begin{bmatrix} J_{\varpi\varpi} & J_{\varpi\boldsymbol{\Phi}:} \\ J^T_{\varpi\boldsymbol{\Phi}:} & J_{\boldsymbol{\Phi}:\boldsymbol{\Phi}:} \end{bmatrix}\begin{bmatrix} \boldsymbol{0} \\ \boldsymbol{v} \end{bmatrix} = \begin{bmatrix} J_{\varpi\boldsymbol{\Phi}:}\boldsymbol{v} \\ J_{\boldsymbol{\Phi}:\boldsymbol{\Phi}:}\boldsymbol{v} \end{bmatrix} = \lambda\begin{bmatrix} \boldsymbol{0} \\ \boldsymbol{v} \end{bmatrix} \quad (\ \boldsymbol{v} \text{ in } \mathcal{N} \text{ or } \mathcal{M}_\perp) \tag{21}$$

This implies that $\boldsymbol{J}$ has $m + m(n-m)$ eigenvectors of the form $[\boldsymbol{0}; \boldsymbol{v}]$, i.e., where mode shape uncertainty is uncoupled from all other parameters.

There remains $(m+1)^2 + m(m-1)$ eigenvalues. They all contribute to mode shape uncertainties in $\mathcal{M}$, i.e., Type 2. To see this, let the eigenvector be partitioned as $\boldsymbol{\theta} = [\boldsymbol{a}; \boldsymbol{b}]$ where $\boldsymbol{a}$ is $(m+1)^2$ dimensional for ϖ and $\boldsymbol{b}$ is mn dimensional for $\boldsymbol{\Phi}$:. Since all eigenvectors of (real-symmetric) $\boldsymbol{J}$ are orthogonal, $\boldsymbol{\theta} = [\boldsymbol{a}; \boldsymbol{b}]$ must be orthogonal to $[\boldsymbol{0}; \boldsymbol{v}]$ where $\boldsymbol{v}$ is in $\mathcal{N}$ or $\mathcal{M}_\perp$. This implies $\boldsymbol{v}^T\boldsymbol{b} = 0$. As $\boldsymbol{v}$ lies in the subspace formed by $\mathcal{N}$ and $\mathcal{M}_\perp$, $\boldsymbol{b}$ must lie in the orthogonal complement of this subspace, i.e., $\mathcal{M}$.

8.5. Condensed eigenvalue problem for Type 2

The eigenvalue properties of Type 2 can be found from an eigenvalue problem of reduced dimension. Essentially, one can represent $\boldsymbol{b}$ in $\boldsymbol{\theta} = [\boldsymbol{a}; \boldsymbol{b}]$ as a linear combination of basis vectors in $\mathcal{M}$, i.e.,

$$\boldsymbol{b} = \begin{bmatrix} \boldsymbol{U}_1\boldsymbol{\alpha}_1 \\ \vdots \\ \boldsymbol{U}_m\boldsymbol{\alpha}_m \end{bmatrix} = \underbrace{\begin{bmatrix} \boldsymbol{U}_1 & & \\ & \ddots & \\ & & \boldsymbol{U}_m \end{bmatrix}}_{\boldsymbol{U}} \underbrace{\begin{bmatrix} \boldsymbol{\alpha}_1 \\ \vdots \\ \boldsymbol{\alpha}_m \end{bmatrix}}_{\boldsymbol{\alpha}} \tag{22}$$

where $\boldsymbol{U}_i$ is a $n \times (m-1)$ matrix containing in its columns the basis $\{\boldsymbol{u}_{ij}\}_{j=1}^{m-1}$ in M but orthogonal to $\boldsymbol{\varphi}_i$ (see Section 7) and $\boldsymbol{\alpha}_i$ is a $(m-1) \times 1$ vector containing the coordinates w.r.t. the basis. Determining $\boldsymbol{b}$ (dim. mn) reduces to determining $\boldsymbol{\alpha}$. An eigenvector of Type 2 can then be represented as

$$\boldsymbol{v} = \begin{bmatrix} \boldsymbol{a} \\ \boldsymbol{U}\boldsymbol{\alpha} \end{bmatrix} = \begin{bmatrix} \boldsymbol{I} & \\ & \boldsymbol{U} \end{bmatrix}\begin{bmatrix} \boldsymbol{a} \\ \boldsymbol{\alpha} \end{bmatrix} \tag{23}$$

For $\boldsymbol{\theta} = [\varpi; \boldsymbol{\Phi}:]$, the eigenvalue problem for $\boldsymbol{J}$ involving eigenvectors of Type 2 reads

$$\begin{bmatrix} J_{\varpi\varpi} & J_{\varpi\boldsymbol{\Phi}:} \\ J_{\boldsymbol{\Phi}:\varpi} & J_{\boldsymbol{\Phi}:\boldsymbol{\Phi}:} \end{bmatrix}\begin{bmatrix} \boldsymbol{I} & \\ & \boldsymbol{U} \end{bmatrix}\begin{bmatrix} \boldsymbol{a} \\ \boldsymbol{\alpha} \end{bmatrix} = \lambda\begin{bmatrix} \boldsymbol{I} & \\ & \boldsymbol{U} \end{bmatrix}\begin{bmatrix} \boldsymbol{a} \\ \boldsymbol{\alpha} \end{bmatrix} \tag{24}$$

Left-multiplying by the transpose of the first matrix on the right hand side gives the generalised eigenvalue problem

$$\boldsymbol{J}_c\boldsymbol{x} = \lambda\boldsymbol{B}\boldsymbol{x} \tag{25}$$

$$\boldsymbol{J}_c = \begin{bmatrix} J_{\varpi\varpi} & J_{\varpi\Phi:}\boldsymbol{U} \\ \boldsymbol{U}^T J_{\Phi:\varpi} & \boldsymbol{U}^T J_{\Phi:\Phi:}\boldsymbol{U} \end{bmatrix} \quad \boldsymbol{B} = \begin{bmatrix} \boldsymbol{I} & \\ & \boldsymbol{U}^T\boldsymbol{U} \end{bmatrix} \quad \boldsymbol{x} = \begin{bmatrix} \boldsymbol{a} \\ \boldsymbol{\alpha} \end{bmatrix} \tag{26}$$

Note that $\boldsymbol{J}_c$ has full rank. The original eigenvalue problem with $\boldsymbol{J}$ of dimension $(m+1)^2 + mn$ is now reduced to one with $\boldsymbol{J}_c$ of dimension $(m+1)^2 + m(m-1)$, which does not depend on the number of measured DOFs n. The complexity w.r.t. n is resolved and consolidated into the associated coordinates in $\boldsymbol{\alpha}$. The eigenvalue properties of $\boldsymbol{J}$ are summarised in Table 3.

8.6. High S/N asymptotic posterior covariance matrix

The asymptotic posterior covariance matrix $\boldsymbol{C}$ is equal to the inverse of the full FIM $\boldsymbol{J}$ ignoring the m zero eigenvalues associated with norm constraints, i.e., evaluated as a pseudo-inverse via eigenvector representation ignoring the zero eigenvalues. It inherits the eigenvectors of $\boldsymbol{J}$ and its eigenvalues are equal to the reciprocal of those of $\boldsymbol{J}$, except for the m zero eigenvalues. It has m zero eigenvalues (Type 0) associated with norm constraints. Another $m(n-m)$ eigenvalues are associated with mode shape uncertainty orthogonal to the MSS (Type 1), equal to $\{\lambda_i^{-1}\}_{i=1}^m$ (each repeating $(n-m)$ times), where $\{\lambda_i\}_{i=1}^m$ are the eigenvalues of $2S_e^{-1}\mathrm{Re}\boldsymbol{\Sigma}\boldsymbol{H}_k$. The remaining $(m+1)^2 + m(m-1)$ eigenvalues are reciprocals of those of the eigenvalue problem in (25). These are non-trivial and are associated potentially with all parameters correlated, i.e., no zeros in the eigenvectors.

9. Dominant mode shape uncertainty

For well-separated modes it has been found in previous studies [23] that mode shape uncertainty is inversely proportional to S/N ratio. Such uncertainty is perpendicular to the mode shape with a variance proportional to the noise PSD. It is therefore typically small for data with good S/N ratio and vanishes for noiseless data, despite the uncertainty in the excitation that remains. Intuitively, for well-separated modes the mode shape values at different DOFs are directly related to their ratio of data FFTs where the effect of the modal force is almost cancelled out when S/N ratio is high. For noiseless data the ratio of data FFTs depends solely on the ratio of mode shape values and hence the latter can be precisely determined (together with a scaling constraint). Except for the zero eigenvalue associated with norm constraint, all other eigenvalues of the mode shape covariance matrix are theoretically the same and hence there is no dominant direction of uncertainty. The foregoing findings in this work reveal that this is not the case for close modes because the $m(m-1)$ eigenvalues associated with uncertainty within MSS (Type 2) are significantly larger than the $m(n-m)$ eigenvalues associated with uncertainty orthogonal to MSS (Type 1). The implication is that for close modes the mode shape uncertainty does not vanish for noiseless data, which is a consequence of the fact that the excitation is not known but modelled in a stochastic manner.

Let $\{\delta_i\}_{i=1}^{mn}$ and $\{\boldsymbol{u}_i\}_{i=1}^{mn}$ be respectively the eigenvalues and eigenvectors of the covariance matrix of $\boldsymbol{\Phi}$:. Given data, $\boldsymbol{\Phi}$: is a Gaussian vector with mean equal to its MPV and uncertain deviation $\Delta\boldsymbol{\Phi}$: given by

$$\Delta\boldsymbol{\Phi} := \begin{bmatrix} \Delta\boldsymbol{\varphi}_1 \\ \vdots \\ \Delta\boldsymbol{\varphi}_m \end{bmatrix} = \sum_{i=1}^{mn} Z_i\sqrt{\delta_i}\boldsymbol{u}_i \tag{27}$$

where $\{Z_i\}_{i=1}^{mn}$ are i.i.d. standard Gaussian random variables. It can be easily verified that the covariance matrix of $\Delta\boldsymbol{\Phi}$: is equal to the mode shape covariance matrix.

The foregoing findings imply that $\boldsymbol{\Phi}$: has $m(m-1)$ dominant uncertain directions within the MSS. The remaining directions are either asymptotically small (orthogonal to MSS, Type 1) for high S/N ratios or norm-constrained (m directions along MPV, Type 0). Analogous results apply to the mode shape $\boldsymbol{\varphi}_i$ $(n \times 1)$ of a particular mode. It has $(m-1)$ dominant uncertain directions within the MSS (Type 2), $(n-m)$ directions orthogonal to the MSS (Type 1) and 1 direction along the MPV that is norm-constrained.

10. Illustrative examples

10.1. Verification

Here we verify numerically the eigenvalue properties of the mode shape FIM predicted in Section 8. Consider two close modes with natural frequencies $f_1 = 1$ Hz and $f_2 = 1.05$ Hz, damping ratios ζ_1 =1% and $\zeta_2 = 1.5\%$, modal force PSDs $S_{11} = S_{22} = 1(\mu\mathrm{g})^2/\mathrm{Hz}$, modal force coherence $\chi = S_{21}/\sqrt{S_{11}S_{22}} = 0.5e^{i\pi/4}$ and mode shapes (confined to measured DOFs) $\boldsymbol{\varphi}_1 = \boldsymbol{u}_1$ and $\boldsymbol{\varphi}_2 = \rho\boldsymbol{u}_1 + \sqrt{1-\rho^2}\boldsymbol{u}_2$ where

$$\boldsymbol{u}_1 = [1 \quad 2 \quad 3 \quad 4 \quad 5]^T/\sqrt{55} \quad \boldsymbol{u}_2 = [1 \quad 2 \quad 3 \quad 0 \quad -14/5]^T/\sqrt{21.48} \tag{28}$$

Check that $\boldsymbol{u}_1$ and $\boldsymbol{u}_2$ are orthogonal unit vectors and the MAC (modal assurance criterion) between $\boldsymbol{\varphi}_1$ and $\boldsymbol{\varphi}_2$ is ρ, which is set to be 0.5. Data is acceleration of 1000 sec duration and sampled at 10 Hz. It is contaminated with white noise of PSD S_e. The latter is set to be $S_e = S_{11}/4\zeta_1^2\gamma$ so that the S/N ratio in terms of PSD at the natural frequency of Mode 1 is γ, which will be varied in the study. The band from 0.9 Hz to 1.1 Hz is used for Bayesian modal ID. This example focuses on verifying the mathematical correctness of the asymptotic FIM in Section 8. The FIMs (asymptotic and exact) are evaluated directly at the actual values of modal properties. In Section 10.2 with field data they will be evaluated at the MPV calculated for given data, which is the best one can do when there is no 'true' parameter value. Nevertheless, to give an idea of how close the modes are in this example, Fig. 4 shows the singular value (SV) spectrum of a typical set of synthetic data when the S/N ratio is 1000.

Here, the number of measured DOFs is $n = 5$ and the number of modes is $m = 2$. The dimension of the mode shape FIM $\boldsymbol{J}_{\boldsymbol{\Phi};\boldsymbol{\Phi}}$ is then $mn = 10$. According to the theory, there are $m = 2$ zero eigenvalues of Type 0 ($\mathcal{N}$) due to norm constraint; $m(n-m) = 6$ eigenvalues of Type 1 ($\mathcal{M}_\perp$) comprising 2 possibly distinct eigenvalues each repeating $n - m = 3$ times; and $m(m-1) = 2$ eigenvalues of Type 2 ($\mathcal{M}$).

Fig. 4(b) shows the eigenvalues of the mode shape FIM $\boldsymbol{J}_{\boldsymbol{\Phi};\boldsymbol{\Phi}}$ based on (3) (circle, 'exact') and the high S/N asymptotic expression in Table 2 (cross, 'asym.'). As the S/N ratio increases, the two sets of values converge to each other, verifying the asymptotic correctness of the latter. Each point of Type 1 in fact contains three visually overlapping points as the eigenvalues of this type repeat three times. The eigenvalues of Type 1 are greater than those of Type 2 by orders of magnitude and increase with S/N ratio because they grow with S_e^{-1} (see $J^{(1)}_{\boldsymbol{\Phi};\boldsymbol{\Phi}}$ in Table 2). The magnitude of Type 2 does not depend on S_e (see $J^{(2)}_{\boldsymbol{\Phi};\boldsymbol{\Phi}}$ in Table 2). A direct implication of this is that Type 1 uncertainty (orthogonal to MSS) will vanish with noiseless data while Type 2 uncertainty (within MSS) will still prevail.

Fig. 5 shows the c.o.v. (coefficient of variation) of frequencies, damping ratios and mode shapes based on the exact (circle) and asymptotic FIM (cross). For the frequencies and damping ratios, the c.o.v. is simply the ratio of posterior standard deviation to MPV. The mode shape c.o.v. is the square root sum of the eigenvalues of the $(n \times n)$ posterior mode shape covariance matrix. For small uncertainty it can be interpreted as the expected value of the hyper angle between the uncertain mode shape and the MPV. As seen in Fig. 5, as the S/N ratio increases, the two values converge to each other, verifying the asymptotic correctness of the asymptotic FIM for high S/N ratio.

10.2. Application to field data

Consider a set of triaxial (x, y, z) ambient acceleration data of 36 h at 50 Hz measured on the roof of Tall building B in [4] during Typhoon Koppu (14 Sep. 2009); see Fig. 6(a). Fig. 1 shows the root PSD and root SV spectra of 30 min data before the main event. The two close modes around 0.18 Hz are translational in nature. Their modal properties were identified (MPV and c.o.v.) previously by BAYOMA using the FFT in the band indicated. The theory in this work offers an opportunity for understanding their ID uncertainty especially in the mode shapes.

10.2.1. Mode shape uncertainty from 30 min data

We first investigate the ID uncertainty of mode shapes using the set of 30 min data. To give a basic idea of modal ID results (MPV, c.o.v.), the frequencies are identified to be 0.184 Hz (0.2%) and 0.189 Hz (0.2%); the damping ratios are 0.54% (30%) and 0.92% (23%). The S/N ratio in terms of PSD at natural frequency is high, about a few thousands, which is also evidenced from Fig. 1.

Given the 30 min data, the full posterior covariance matrix comprising all parameters is calculated. The 3×3 posterior covariance matrix of each mode shape is taken from the corresponding partition in the full covariance matrix. The results are shown in Table 5. The type indicated below each eigenvalue is determined based on the direction of the eigenvector.

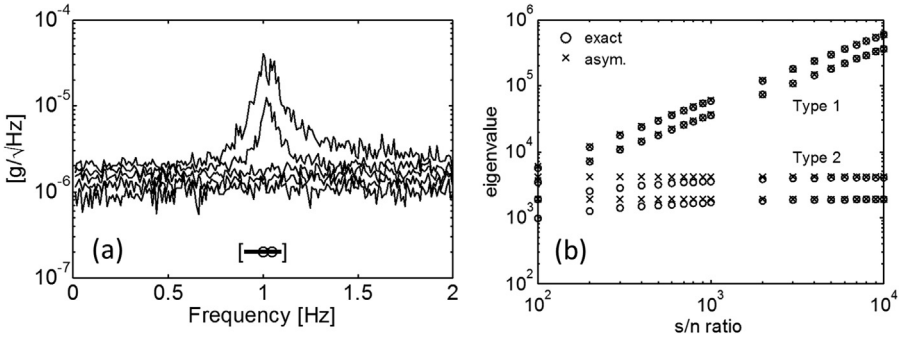

Fig. 4. (a) Root SV spectrum of a typical set of synthetic data; (b) Eigenvalues of mode shape FIM $\boldsymbol{J}_{\boldsymbol{\Phi};\boldsymbol{\Phi}}$. Circle – exact based on (3); cross – high S/N asymptotic value based on Table 2. The spectrum in (a) has been averaged for visualisation and hence has a lower resolution than the 'raw' FFT (i.e., no averaging) used in BAYOMA.

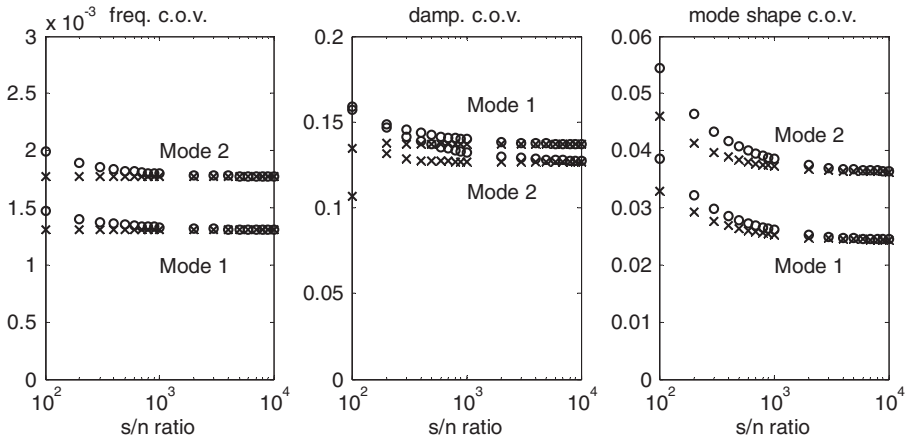

Fig. 5. Comparison of c.o.v. based on exact FIM (circle) and asymptotic FIM (cross).

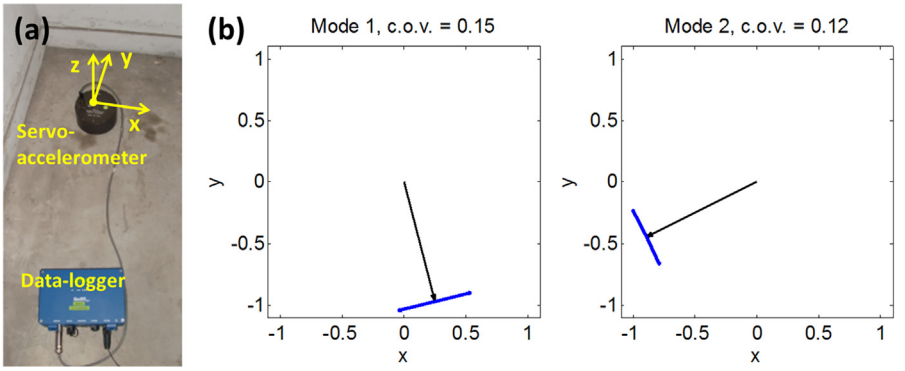

Fig. 6. (a) Sensor and data logger. (b) MPV of mode shapes (black, pointing from origin) and ±two-sigma uncertainty (blue) of Type 2. (For interpretation of the references to colour in this figure legend, the reader is referred to the web version of this article.)

For Mode 1, the eigenvalue 8.39e−7 has a MAC of practically 1 with the most probable mode shape and so it corresponds to Type 0 (norm-constrained). Its value is not exactly zero due to numerical errors, which is typical. While the other two eigenvectors have a MAC of practically zero with the most probable mode shape, the one with eigenvalue 8.21e−9 is also orthogonal to Mode 2, and so it corresponds to Type 1 (uncertainty orthogonal to MSS). This eigenvalue is not theoretically zero, but is inversely proportional to the S/N ratio. It can be smaller than the calculated eigenvalue of Type 0 when the S/N ratio is high, as in the present case. The remaining eigenvector with eigenvalue 2.16e−2 corresponds to Type 2 (uncertainty within MSS). Summing the eigenvalues and taking square root gives a mode shape c.o.v. of 15%, which is clearly dominated by Type 2. Similar observations apply to Mode 2, which has a c.o.v. of 12%. It should be noted that before this work the mode shape covariance matrix can be calculated numerically but there is little or no insight on why such values are obtained. Based on the theory in this work we are now able to understand why the results turn out the way they appear. For example, there should be no surprise now why in Table 5 the largest eigenvalue is several orders of magnitude larger than the second eigenvalue – it is of Type 2 that does not diminish with the quality of data. Without the theory in this work one may wonder if this is due to numerical error. The large disparity in Type 1 and 2 also suggests that one can simply focus on Type 2 uncertainty, which is confined within the mode shape subspace with dimension often much smaller than the whole space.

Table 5
Eigenvalues of mode shape covariance matrix and mode shape c.o.v.

Mode	Eigenvalues			c.o.v.
1	8.21e−9 (Type 1)	8.39e−7 (Type 0)	2.16e−2 (Type 2)	15%
2	6.01e−9 (Type 1)	6.27e−7 (Type 0)	1.47e−2 (Type 2)	12%

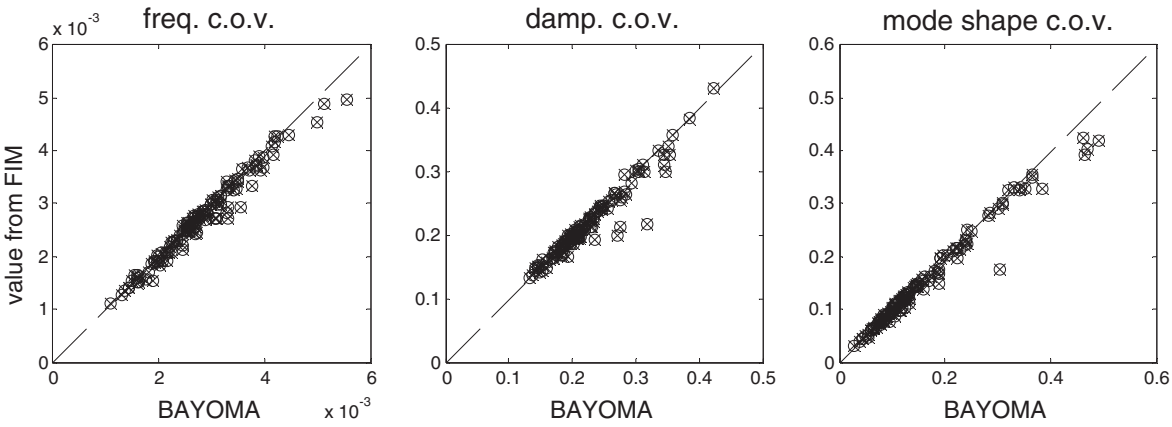

Fig. 7. Comparison of posterior c.o.v. from BAYOMA (for given data) and FIM. Cross ('x') – based on high S/N asymptotic FIM (Table 2), circle ('o') – based on exact FIM (3). Each point refers to the result of 30 min data out of 36 h (so total 72 points).

Fig. 6(b) shows the most probable mode shapes with an arrow pointing from the origin. The two mode shapes have a MAC of 0.21 and so they are not orthogonal. The blue arrows show the '± two-sigma' uncertain mode shape deviation of the largest eigenvalue (Type 2), i.e., two times the term $\sqrt{\delta_i}\boldsymbol{u}_i$ in (27). Only the xy view is shown because the mode shape component along the z direction is negligible. The principal mode shape deviations are roughly tangential to the unit circle, which is consistent with the fact that the mode shapes have unit length (in the unit sphere).

10.3. Comparison of c.o.v. from asymptotic FIM, exact FIM and BAYOMA

We next compare the values of posterior c.o.v. based on the high S/N asymptotic FIM (Table 2), exact FIM (Eq. (3)) and BAYOMA ([22], for given data). For this purpose we divide the 36 h data into non-overlapping windows of 30 min and identify the modal properties of the two modes (MPV and c.o.v.) using BAYOMA. The high S/N asymptotic FIM and exact FIM are then calculated using the MPV (the best one can do, since there is no 'true' value). The pseudo-inverse of these matrices (ignoring zero eigenvalues from norm constraints) gives the covariance matrix, from which the c.o.v. can be obtained. Fig. 7 summarises the results (Modes 1 and 2 are not distinguished). The c.o.v. values of BAYOMA are plotted on the x-axis. The c.o.v. values from FIM are plotted on the y-axis, with the crosses for the high S/N asymptotic FIM and circles for the exact FIM. The crosses and circles almost overlap, which is consistent with the fact that the S/N ratio of data is quite high (at least a few thousands). The crosses and circles do not lie along the 1:1 dashed line, indicating a discrepancy between the c.o.v. from FIM and BAYOMA. This does not discredit the FIM or the high S/N asymptotic FIM, as the c.o.v. from BAYOMA is for a given data set and it always has a random part, though theoretically negligible for long data and assuming no modelling error and existence of 'true' parameter values. The discrepancy may reveal scenarios of modelling error, e.g., non-flat spectrum or non-classical damping, although there is little understanding about this aspect. More comparison and discussion about the meaning of ID uncertainty based on the exact FIM and BAYOMA can be found in [28]. Recognising that the x-axis is the uncertainty we can only calculate for given data (but no insight) and the y-axis (cross) is the uncertainty we can explain in the context of structural dynamics, the clustering of points around the 1:1 lines in Fig. 7 represents an important progress in our understanding of ID uncertainty in close modes.

11. Conclusions

This work has performed an analytical study on the ID uncertainty of close modes that contributes to its understanding and provides a pathway for development of explicit formulae governing uncertainty, i.e., 'uncertainty law', in the future. The basic assumptions in the ID model include linear dynamics with classically damped modes, stationary modal excitations with constant PSD matrix within resonance band and stationary noise i.i.d. among measured DOFs with a constant PSD within the resonance band. Data is assumed to be sufficiently long in the sense that the number of FFT points in the resonance band is large compared to 1 (see Section 4); and has high S/N ratio (see (47)).

Before this work it was possible to calculate the posterior covariance matrix for given data using a Bayesian modal ID algorithm (BAYOMA) but it had not been possible to develop insights such as can be realised for well-separated modes. The large size of the matrix and its lack of sparseness, i.e., all parameters (except the noise PSD) are significantly correlated, has been identified as the cause. This work has discovered analytically the intrinsic correlation structure of the covariance matrix for long data and high S/N ratio, supported by mathematical proof, numerical verification and application with field data. The high S/N asymptotic expressions of Fisher Information Matrix (FIM, Table 2) and the analytical eigenvalue properties (Table 3) discovered are milestones for developing uncertainty laws for close modes that allow one to master the iden-

tification uncertainty and manage in ambient vibration tests. While the dimension of the posterior covariance matrix grows linearly with the number of measured DOFs, the theory in this work has reduced it to one independent of the number. The complexity w.r.t. the measured DOFs, which has been one of the major hurdles, has been resolved.

Mode shape uncertainty in well-separated modes is often negligible as it diminishes with increased data quality. This work has shown that the same is not true for close modes, where for each mode there is significant uncertainty within the mode shape subspace (MSS). Intuitively the mode shapes can 'trade' their directions within the MSS to give a similar likelihood value in Bayesian inference (or 'data fit' in non-Bayesian methods), and hence is less distinguishable. Such uncertainty does not diminish even for noiseless data. This puts a limit on the achievable precision of OMA with close modes. This mode shape uncertainty potentially correlates with all other parameters. Understanding such correlation structure requires yet another level of advance in the theory.

This work has not reached the ultimate goal of 'uncertainty law', i.e., explicitly relating ID uncertainty to test configuration for understanding and test planning, but the analytical expressions of FIM (Table 2) and understanding about its eigenvalue properties (Table 3) shed light on possibility and provide the pathway to it. Obtaining the uncertainty law will require further analytical investigation on the FIM and its inverse to produce explicit and manageable expressions for the posterior variances of modal properties – a big challenge, considering the large dimension of the FIM and entangling of modes.

Acknowledgements

This work is part of a research project on "Uncertainty quantification and management in ambient modal identification" funded by the Engineering and Physical Sciences Research Council (grant EP/N017897/1 and EP/N017803/1) to understand ID uncertainty and provide a strong scientific basis for implementing and planning ambient vibration tests. The research materials supporting this publication can be accessed by contacting ivanau@ntu.edu.sg.

Appendix A. Derivation of J_{xy}, J_{xS_e} and $J_{S_eS_e}$ ($x, y = f, \zeta, \boldsymbol{S}$) in Table 2

The expressions can be derived by substituting the Taylor expansion of $\boldsymbol{E}_k^{-1}$ from (9) and the derivatives in (11) into (3), evaluating terms of increasing order and retaining the leading order term. The expression of $J_{S_eS_e}$ is obtained by replacing $\boldsymbol{E}_k^{-1}$ by its 0th order term, i.e., $\boldsymbol{Q}$, using $\boldsymbol{E}_k^{(S_e)} = \boldsymbol{I}_m$ in (11) and noting that $tr(\boldsymbol{QQ}) = tr(\boldsymbol{Q}) = n - m$.

For J_{xy}, since $\boldsymbol{E}_k^{-1}$ appears twice in (3), the 0th order of J_{xy} involves the 0th × 0th order of $\boldsymbol{E}_k^{-1}$. Since the 0th order of $\boldsymbol{E}_k^{-1}$ is $\boldsymbol{Q}$ and $\boldsymbol{Q}\overline{\boldsymbol{\Phi}} = \overline{\boldsymbol{\Phi}}^T\boldsymbol{Q} = \boldsymbol{0}$, the 0th order of J_{xy} is zero. The 1st order of J_{xy} involves the 0th × 1st order +1st × 0th order of $\boldsymbol{E}_k^{-1}$. For the same reason as before, these terms are zero. The 2nd order of J_{xy} involves the 0th × 2nd + 1st × 1st order of $\boldsymbol{E}_k^{-1}$. The former is zero. The latter is not zero and hence is the leading order of J_{xy} as given in Table 2. To obtain the expression, note that

$$(\text{1st order of } \boldsymbol{E}_k^{-1}) \times \boldsymbol{E}_k^{(x)} = (S_e^{-1}\boldsymbol{R}^T\boldsymbol{\varepsilon}_k\boldsymbol{R})(\overline{\boldsymbol{\Phi}}\boldsymbol{H}_k^{(x)}\overline{\boldsymbol{\Phi}}^T) = \boldsymbol{R}^T\boldsymbol{H}_k^{-1}\boldsymbol{H}_k^{(x)}\overline{\boldsymbol{\Phi}}^T \tag{29}$$

since $\boldsymbol{R}\overline{\boldsymbol{\Phi}} = \boldsymbol{I}_m$ and $\boldsymbol{\varepsilon}_k = S_e\boldsymbol{H}_k^{-1}$. This gives the expression in Table 2:

$$J_{xy} \sim tr\boldsymbol{\Sigma}(\boldsymbol{R}^T\boldsymbol{H}_k^{-1}\boldsymbol{H}_k^{(x)}\overline{\boldsymbol{\Phi}}^T)(\boldsymbol{R}^T\boldsymbol{H}_k^{-1}\boldsymbol{H}_k^{(y)}\overline{\boldsymbol{\Phi}}^T) = tr\boldsymbol{\Sigma}\boldsymbol{H}_k^{-1}\boldsymbol{H}_k^{(x)}\boldsymbol{H}_k^{-1}\boldsymbol{H}_k^{(y)} \tag{30}$$

where we have used the cyclic property of trace ($tr(AB) = tr(BA)$) to move the $\overline{\boldsymbol{\Phi}}^T$ on the right end to the left end and then $\overline{\boldsymbol{\Phi}}^T\boldsymbol{R}^T = (\boldsymbol{R}\overline{\boldsymbol{\Phi}})^T = \boldsymbol{I}_m$ to simplify.

Applying the same argument above to J_{xS_e} shows that its leading order is also the 1st × 1st order of $\boldsymbol{E}_k^{-1}$. Using (29),

$$J_{xS_e} \sim tr\boldsymbol{\Sigma}(\boldsymbol{R}^T\boldsymbol{H}_k^{-1}\boldsymbol{H}_k^{(x)}\overline{\boldsymbol{\Phi}}^T)(S_e^{-1}\boldsymbol{R}^T\boldsymbol{\varepsilon}_k\boldsymbol{R}) = tr\boldsymbol{\Sigma}(\overline{\boldsymbol{\Phi}}^T\overline{\boldsymbol{\Phi}})^{-1}\boldsymbol{H}_k^{-1}\boldsymbol{H}_k^{(x)}\boldsymbol{H}_k^{-1} \tag{31}$$

where we have used the cyclic property of trace to move the $\boldsymbol{R}$ on the right end to the left end; then $\boldsymbol{R}\boldsymbol{R}^T = (\overline{\boldsymbol{\Phi}}^T\overline{\boldsymbol{\Phi}})^{-1}$, $\overline{\boldsymbol{\Phi}}^T\boldsymbol{R}^T = \boldsymbol{I}_m$ and $\boldsymbol{\varepsilon}_k = S_e\boldsymbol{H}_k^{-1}$ to simplify.

Appendix B. Derivation of (13)–(15) in Section 6

Substituting (11) and (12) into (3) gives

$$J_{x\Phi_{ri}} = tr\boldsymbol{\Sigma}\boldsymbol{E}_k^{-1}\left(\overline{\boldsymbol{\Phi}}\boldsymbol{H}_k^{(x)}\overline{\boldsymbol{\Phi}}^T\right)\boldsymbol{E}_k^{-1}\left(\overline{\boldsymbol{\Phi}}^{(\Phi_{ri})}\boldsymbol{H}_k\overline{\boldsymbol{\Phi}}^T + \overline{\boldsymbol{\Phi}}\boldsymbol{H}_k\overline{\boldsymbol{\Phi}}^{(\Phi_{ri})T}\right) \qquad x = f, \zeta, \boldsymbol{S} \tag{32}$$

$$J_{S_e\Phi_{ri}} = tr\boldsymbol{\Sigma}\boldsymbol{E}_k^{-2}\left(\overline{\boldsymbol{\Phi}}^{(\Phi_{ri})}\boldsymbol{H}_k\overline{\boldsymbol{\Phi}}^T + \overline{\boldsymbol{\Phi}}\boldsymbol{H}_k\overline{\boldsymbol{\Phi}}^{(\Phi_{ri})}\right) \tag{33}$$

$$J_{xy} = tr\boldsymbol{\Sigma}\boldsymbol{E}_k^{-1}\left(\overline{\boldsymbol{\Phi}}^{(x)}\boldsymbol{H}_k\overline{\boldsymbol{\Phi}}^T + \overline{\boldsymbol{\Phi}}\boldsymbol{H}_k\overline{\boldsymbol{\Phi}}^{(x)T}\right)\boldsymbol{E}_k^{-1}\left(\overline{\boldsymbol{\Phi}}^{(y)}\boldsymbol{H}_k\overline{\boldsymbol{\Phi}}^T + \overline{\boldsymbol{\Phi}}\boldsymbol{H}_k\overline{\boldsymbol{\Phi}}^{(y)T}\right) \qquad x, y = \boldsymbol{\Phi} \tag{34}$$

Using (56) and (57) in Appendix D to simplify gives

$$J_{x\Phi_{ri}} = 2\mathrm{Re}tr\Sigma \boldsymbol{E}_k^{-1}\overline{\boldsymbol{\Phi}}\boldsymbol{H}_k^{(x)}\overline{\boldsymbol{\Phi}}^T\boldsymbol{E}_k^{-1}\overline{\boldsymbol{\Phi}}^{(\Phi_{ri})}\boldsymbol{H}_k\overline{\boldsymbol{\Phi}}^T \qquad x = f, \zeta, \boldsymbol{S} \tag{35}$$

$$J_{S_e\Phi_{ri}} = 2\mathrm{Re}tr\Sigma \boldsymbol{E}_k^{-2}\overline{\boldsymbol{\Phi}}^{(\Phi_{ij})}\boldsymbol{H}_k\overline{\boldsymbol{\Phi}}^T \tag{36}$$

$$J_{xy} = 2\mathrm{Re}tr\Sigma \boldsymbol{E}_k^{-1}\overline{\boldsymbol{\Phi}}^{(x)}\boldsymbol{H}_k\overline{\boldsymbol{\Phi}}^T\boldsymbol{E}_k^{-1}(\overline{\boldsymbol{\Phi}}^{(y)}\boldsymbol{H}_k\overline{\boldsymbol{\Phi}}^T + \overline{\boldsymbol{\Phi}}\boldsymbol{H}_k\overline{\boldsymbol{\Phi}}^{(y)T}) \qquad x, y = \boldsymbol{\Phi} \tag{37}$$

Substituting the Taylor expansion of $\boldsymbol{E}_k^{-1}$ from (9) and taking the leading order term gives (13)–(15). Details are presented separately in Appendix B.1–B.3 below.

B.1. $J_{x\Phi_{ri}}$ in (13) for $x = f, \zeta, \boldsymbol{S}$

Substituting (9) into (35) gives the following terms of different orders:

0th order of $J_{x\Phi_{ri}}$ involves 0th × 0th order of $\boldsymbol{E}_k^{-1}$

1st order of $J_{x\Phi_{ri}}$ involves 0th × 1st + 1st × 0th order of $\boldsymbol{E}_k^{-1}$

2nd order of $J_{x\Phi_{ri}}$ involves 0th × 2nd + 2nd × 0th + 1st × 1st order of $\boldsymbol{E}_k^{-1}$

Due to the property of $\boldsymbol{Q}$, any product involving the 0th order of $\boldsymbol{E}_k^{-1}$ gives zero. This implies that the 0th and 1st order of $J_{x\Phi_{ri}}$ is zero. The leading order of $J_{x\Phi_{ri}}$ is then the second order term involving the 1st × 1st order of $\boldsymbol{E}_k^{-1}$. Evaluating it gives the expression in (13):

$$J_{x\Phi_{ri}} \sim 2S_e^{-2}\mathrm{Re}tr\Sigma(\boldsymbol{R}^T\boldsymbol{\varepsilon}_k\boldsymbol{R})(\overline{\boldsymbol{\Phi}}\boldsymbol{H}_k^{(x)}\overline{\boldsymbol{\Phi}}^T)(\boldsymbol{R}^T\boldsymbol{\varepsilon}_k\boldsymbol{R})(\overline{\boldsymbol{\Phi}}^{(\Phi_{ri})}\boldsymbol{H}_k\overline{\boldsymbol{\Phi}}^T) = 2\mathrm{Re}tr\Sigma[\boldsymbol{H}_k^{(x)}\boldsymbol{H}_k^{-1}\boldsymbol{R}\overline{\boldsymbol{\Phi}}^{(\Phi_{ri})}] \tag{38}$$

where we have used the cyclic property of trace to move $\boldsymbol{H}_k\overline{\boldsymbol{\Phi}}^T$ on the right end to the left end; then $\overline{\boldsymbol{\Phi}}^T\boldsymbol{R}^T = \boldsymbol{I}_m$ and $\boldsymbol{\varepsilon}_k = S_e\boldsymbol{H}_k^{-1}$ to simplify.

B.2. $J_{S_e\Phi_{ri}}$ in (14)

Using $\boldsymbol{E}_k^{-1}$ from (9) and expanding the square of $\boldsymbol{E}_k^{-2} = (\boldsymbol{E}_k^{-1})^2$ gives terms of different order. The 0th order of $\boldsymbol{E}_k^{-2}$ is $S_e^{-2}\boldsymbol{Q}$ because $\boldsymbol{Q}^2 = \boldsymbol{Q}$. Replacing $\boldsymbol{E}_k^{-2}$ in (36) by $S_e^{-2}\boldsymbol{Q}$ and using the cyclic property of trace and $\overline{\boldsymbol{\Phi}}^T\boldsymbol{Q} = \boldsymbol{0}$ gives a zero vector. The leading order of $J_{S_e\Phi_{ri}}$ should then come from the higher order terms of $\boldsymbol{E}_k^{-2}$. The 1st order of $\boldsymbol{E}_k^{-2}$ comes from the 0th × 1st and 1st × 0th order term of $\boldsymbol{E}_k^{-1}$. Using $\boldsymbol{Q}\overline{\boldsymbol{\Phi}} = \overline{\boldsymbol{\Phi}}^T\boldsymbol{Q} = \boldsymbol{0}$ shows that they are all zero. The next higher order term of $\boldsymbol{E}_k^{-2}$ is the 2nd order given by the 1st × 1st order term of $\boldsymbol{E}_k^{-1}$:

$$\boldsymbol{E}_k^{-2} \sim S_e^{-2}(\boldsymbol{R}^T\boldsymbol{\varepsilon}_k\boldsymbol{R})(\boldsymbol{R}^T\boldsymbol{\varepsilon}_k\boldsymbol{R}) = S_e^{-2}\boldsymbol{R}^T\boldsymbol{\varepsilon}_k(\overline{\boldsymbol{\Phi}}^T\overline{\boldsymbol{\Phi}})^{-1}\boldsymbol{\varepsilon}_k\boldsymbol{R} \tag{39}$$

since $\boldsymbol{R}\boldsymbol{R}^T = (\overline{\boldsymbol{\Phi}}^T\overline{\boldsymbol{\Phi}})^{-1}$. Substituting into (36) gives

$$J_{S_e\Phi_{ri}} \sim 2S_e^{-2}\mathrm{Re}tr\Sigma[\boldsymbol{R}^T\boldsymbol{\varepsilon}_k(\overline{\boldsymbol{\Phi}}^T\overline{\boldsymbol{\Phi}})^{-1}\boldsymbol{\varepsilon}_k\boldsymbol{R}\overline{\boldsymbol{\Phi}}^{(\Phi_{ri})}\boldsymbol{H}_k\overline{\boldsymbol{\Phi}}^T] = 2\mathrm{Re}tr\Sigma[(\overline{\boldsymbol{\Phi}}^T\overline{\boldsymbol{\Phi}})^{-1}\boldsymbol{H}_k^{-1}\boldsymbol{R}\overline{\boldsymbol{\Phi}}^{(\Phi_{ri})}] \tag{40}$$

where we have used the cyclic property of trace to move $\boldsymbol{H}_k\overline{\boldsymbol{\Phi}}^T$ on the right end to the left end; then $\overline{\boldsymbol{\Phi}}^T\boldsymbol{R}^T = \boldsymbol{I}_m$ and $\boldsymbol{\varepsilon}_k = S_e\boldsymbol{H}_k^{-1}$ to simplify.

B.3. J_{xy} in (15) for $x, y = \boldsymbol{\Phi}$

Substituting (9) into (37) gives the 0th, 1st and 2nd order terms of J_{xy}, which are denoted by $J_{xy}^{(0)}, J_{xy}^{(1)}$ and $J_{xy}^{(2)}$, respectively. The 0th order $J_{xy}^{(0)}$ involves the 0th × 0th order of $\boldsymbol{E}_k^{-1}$. Replacing $\boldsymbol{E}_k^{-1}$ by its 0th order $\boldsymbol{Q}$ and expanding gives

$$J_{xy}^{(0)} = 2S_e^{-2}\mathrm{Re}tr\Sigma[\boldsymbol{Q}\overline{\boldsymbol{\Phi}}^{(x)}\boldsymbol{H}_k\overline{\boldsymbol{\Phi}}^T\boldsymbol{Q}\overline{\boldsymbol{\Phi}}^{(y)}\boldsymbol{H}_k\overline{\boldsymbol{\Phi}}^T + \boldsymbol{Q}\overline{\boldsymbol{\Phi}}^{(x)}\boldsymbol{H}_k\overline{\boldsymbol{\Phi}}^T\boldsymbol{Q}\overline{\boldsymbol{\Phi}}\boldsymbol{H}_k\overline{\boldsymbol{\Phi}}^{(y)T}] = 0 \tag{41}$$

because the trace of both terms are zero: for the first term, use the cyclic property of trace to move $\overline{\boldsymbol{\Phi}}^T$ on the right end to the left end and find $\overline{\boldsymbol{\Phi}}^T\boldsymbol{Q} = \boldsymbol{0}$; the second term has $\boldsymbol{Q}\overline{\boldsymbol{\Phi}} = \boldsymbol{0}$.

Next, $J_{xy}^{(1)}$ involves the 0th × 1st + 1st × 0th order of $\boldsymbol{E}_k^{-1}$. The latter can be seen to be zero after using $\overline{\boldsymbol{\Phi}}^T\boldsymbol{Q} = \boldsymbol{0}$. Thus $J_{xy}^{(1)}$ only involves the 0th × 1st order of $\boldsymbol{E}_k^{-1}$:

$$\begin{aligned} J_{xy}^{(1)} &= 2S_e^{-2}\mathrm{Re}tr\Sigma[\boldsymbol{Q}\overline{\boldsymbol{\Phi}}^{(x)}\boldsymbol{H}_k\overline{\boldsymbol{\Phi}}^T(\boldsymbol{R}^T\boldsymbol{\varepsilon}_k\boldsymbol{R})(\overline{\boldsymbol{\Phi}}^{(y)}\boldsymbol{H}_k\overline{\boldsymbol{\Phi}}^T + \overline{\boldsymbol{\Phi}}\boldsymbol{H}_k\overline{\boldsymbol{\Phi}}^{(y)T})] \\ &= 2S_e^{-1}\mathrm{Re}tr\Sigma[\boldsymbol{Q}\overline{\boldsymbol{\Phi}}^{(x)}\boldsymbol{R}(\overline{\boldsymbol{\Phi}}^{(y)}\boldsymbol{H}_k\overline{\boldsymbol{\Phi}}^T + \overline{\boldsymbol{\Phi}}\boldsymbol{H}_k\overline{\boldsymbol{\Phi}}^{(y)T})] \end{aligned} \tag{42}$$

after using $\overline{\boldsymbol{\Phi}}^T\boldsymbol{R}^T = \boldsymbol{I}_m$ and $\boldsymbol{\varepsilon}_k = S_e\boldsymbol{H}_k^{-1}$. Multiplying gives two terms. For the first term, use the cyclic property of trace to move $\overline{\boldsymbol{\Phi}}^T$ on the right end to the left end; then use $\overline{\boldsymbol{\Phi}}^T\boldsymbol{Q} = \boldsymbol{0}$ to see that the first term is zero. This leaves the second term as the expression in (16):

$$J_{xy}^{(1)} \sim 2S_e^{-1}\mathrm{Re}tr\Sigma[\boldsymbol{Q}\overline{\boldsymbol{\Phi}}^{(x)}\boldsymbol{R}\overline{\boldsymbol{\Phi}}\boldsymbol{H}_k\overline{\boldsymbol{\Phi}}^{(y)T}] = 2S_e^{-1}tr[\boldsymbol{Q}\overline{\boldsymbol{\Phi}}^{(x)}(\mathrm{Re}\Sigma\boldsymbol{H}_k)\overline{\boldsymbol{\Phi}}^{(y)T}] \tag{43}$$

after using $\boldsymbol{R}\overline{\boldsymbol{\Phi}} = \boldsymbol{I}_m$ and carrying $\mathrm{Re}\Sigma$ inside.

Finally, $J_{xy}^{(2)}$ involves the 0th × 2nd + 1st × 1st + 2nd × 0th of $\boldsymbol{E}_k^{-1}$. Substituting into (37) and simplifying shows that the 2nd × 0th term is zero. Using similar arguments as before,

$$\begin{aligned}
&0\,\mathrm{th}\times 2\,\mathrm{nd}\,\mathrm{term}\\
&= -2S_e^{-2}\mathrm{Re}tr\Sigma[\boldsymbol{Q}(\overline{\boldsymbol{\Phi}}^{(x)}\boldsymbol{H}_k\overline{\boldsymbol{\Phi}}^T)(\boldsymbol{R}^T\boldsymbol{\varepsilon}_k(\overline{\boldsymbol{\Phi}}^T\overline{\boldsymbol{\Phi}})^{-1}\boldsymbol{\varepsilon}_k\boldsymbol{R})(\overline{\boldsymbol{\Phi}}^{(y)}\boldsymbol{H}_k\overline{\boldsymbol{\Phi}}^T + \overline{\boldsymbol{\Phi}}\boldsymbol{H}_k\overline{\boldsymbol{\Phi}}^{(y)T})]\\
&= -2S_e^{-1}\mathrm{Re}tr\Sigma[\boldsymbol{Q}\overline{\boldsymbol{\Phi}}^{(x)}(\overline{\boldsymbol{\Phi}}^T\overline{\boldsymbol{\Phi}})^{-1}\boldsymbol{\varepsilon}_k\boldsymbol{R}(\overline{\boldsymbol{\Phi}}^{(y)}\boldsymbol{H}_k\overline{\boldsymbol{\Phi}}^T + \overline{\boldsymbol{\Phi}}\boldsymbol{H}_k\overline{\boldsymbol{\Phi}}^{(y)T})]\\
&= -2N_f tr[\boldsymbol{Q}\overline{\boldsymbol{\Phi}}^{(x)}(\overline{\boldsymbol{\Phi}}^T\overline{\boldsymbol{\Phi}})^{-1}\overline{\boldsymbol{\Phi}}^{(y)T}]
\end{aligned} \tag{44}$$

where the trace of the first term in the second equality is zero;

$$\begin{aligned}
&1\,\mathrm{st}\times 1\mathrm{st}\,\mathrm{term}\\
&= 2S_e^{-2}\mathrm{Re}tr\Sigma(\boldsymbol{R}^T\boldsymbol{\varepsilon}_k\boldsymbol{R})(\overline{\boldsymbol{\Phi}}^{(x)}\boldsymbol{H}_k\overline{\boldsymbol{\Phi}}^T)(\boldsymbol{R}^T\boldsymbol{\varepsilon}_k\boldsymbol{R})(\overline{\boldsymbol{\Phi}}^{(y)}\boldsymbol{H}_k\overline{\boldsymbol{\Phi}}^T + \overline{\boldsymbol{\Phi}}\boldsymbol{H}_k\overline{\boldsymbol{\Phi}}^{(y)T})\\
&= 2S_e^{-1}\mathrm{Re}tr\Sigma[\boldsymbol{R}^T\boldsymbol{\varepsilon}_k\boldsymbol{R}\overline{\boldsymbol{\Phi}}^{(x)}\boldsymbol{R}(\overline{\boldsymbol{\Phi}}^{(y)}\boldsymbol{H}_k\overline{\boldsymbol{\Phi}}^T + \overline{\boldsymbol{\Phi}}\boldsymbol{H}_k\overline{\boldsymbol{\Phi}}^{(y)T})]\\
&= 2N_f tr[\boldsymbol{R}\overline{\boldsymbol{\Phi}}^{(x)}\boldsymbol{R}\overline{\boldsymbol{\Phi}}^{(y)}] + 2\mathrm{Re}tr\Sigma[\boldsymbol{R}^T\boldsymbol{H}_k^{-1}\boldsymbol{R}\overline{\boldsymbol{\Phi}}^{(x)}\boldsymbol{H}_k\overline{\boldsymbol{\Phi}}^{(y)T}]
\end{aligned} \tag{45}$$

after expanding and using the cyclic property of trace. Combining (44) and (45),

$$J_{xy}^{(2)} = -2N_f tr[\boldsymbol{Q}\overline{\boldsymbol{\Phi}}^{(x)}(\overline{\boldsymbol{\Phi}}^T\overline{\boldsymbol{\Phi}})^{-1}\overline{\boldsymbol{\Phi}}^{(y)T}] + 2N_f tr[\boldsymbol{R}\overline{\boldsymbol{\Phi}}^{(x)}\boldsymbol{R}\overline{\boldsymbol{\Phi}}^{(y)}] + 2\mathrm{Re}tr\Sigma[\boldsymbol{R}^T\boldsymbol{H}_k^{-1}\boldsymbol{R}\overline{\boldsymbol{\Phi}}^{(x)}\boldsymbol{H}_k\overline{\boldsymbol{\Phi}}^{(y)T}] \tag{46}$$

Note that $J_{xy}^{(1)}$ in (43) and the first term in (46) both contain $\boldsymbol{Q}\overline{\boldsymbol{\Phi}}^{(x)}$ on the left and $\overline{\boldsymbol{\Phi}}^{(y)T}$ on the right. Assume that the modes are 'sufficiently linearly independent' in the sense that (e.g., in terms of eigenvalues)

$$S_e(N_f^{-1}\mathrm{Re}\Sigma\boldsymbol{H}_k)^{-1}(\overline{\boldsymbol{\Phi}}^T\overline{\boldsymbol{\Phi}})^{-1} \ll \boldsymbol{I}_m \tag{47}$$

In this case the first term in (46) is negligible compared to $J_{xy}^{(1)}$. Omitting it gives (17).

Appendix C. Derivation of $J_{x\boldsymbol{\varphi}_i}$, $J_{S_e\boldsymbol{\Phi}_i}$ and $J_{\boldsymbol{\Phi}:\boldsymbol{\Phi}:}$ in Table 2

C.1. $J_{x\boldsymbol{\varphi}_i}$ and $J_{S_e\boldsymbol{\varphi}_i}$

The steps for deriving $J_{x\boldsymbol{\varphi}_i}$ and $J_{S_e\boldsymbol{\varphi}_i}$ are the same so here we consider $J_{x\boldsymbol{\varphi}_i}$ only. Substituting (18) with $||\boldsymbol{\varphi}_i|| = 1$ into (13) and carrying the summation inside,

$$J_{x\Phi_{ri}} \sim 2tr\left[(\mathrm{Re}\Sigma\boldsymbol{H}_k^{(x)}\boldsymbol{H}_k^{-1})\boldsymbol{R}(\boldsymbol{I}_n - \overline{\boldsymbol{\varphi}}_i\overline{\boldsymbol{\varphi}}_i^T)\boldsymbol{e}_r\boldsymbol{e}_i^T\right] \tag{48}$$

Using the cyclic property of trace to move $\boldsymbol{e}_i^T$ to the left end so that the product inside $tr(\cdot)$ becomes a scalar, we obtain

$$J_{x\Phi_{ri}} \sim 2\boldsymbol{e}_i^T\left(\mathrm{Re}\Sigma\boldsymbol{H}_k^{(x)}\boldsymbol{H}_k^{-1}\right)\boldsymbol{R}(\boldsymbol{I}_n - \overline{\boldsymbol{\varphi}}_i\overline{\boldsymbol{\varphi}}_i^T)\boldsymbol{e}_r \tag{49}$$

Assembling $J_{x\boldsymbol{\varphi}_i} = [J_{x\Phi_{1i}}, \ldots, J_{x\Phi_{ni}}]$ and noting $[\boldsymbol{e}_1, \ldots, \boldsymbol{e}_n] = \boldsymbol{I}_n$ and $\boldsymbol{R}(\boldsymbol{I}_n - \overline{\boldsymbol{\varphi}}_i\overline{\boldsymbol{\varphi}}_i^T) = \boldsymbol{Q}_i$ gives the expression in Table 2.

C.2. $J_{\boldsymbol{\Phi}:\boldsymbol{\Phi}:}^{(1)}$ in Table 2

Consider $J_{\Phi_{ri}\Phi_{sj}}^{(1)}$, i.e., J_{xy} in (16) with $x = \Phi_{ri}$ and $y = \Phi_{sj}$:

$$J_{\Phi_{ri}\Phi_{sj}}^{(1)} \sim 2S_e^{-1}tr[\boldsymbol{Q}\overline{\boldsymbol{\Phi}}^{(\Phi_{ri})}(\mathrm{Re}\Sigma\boldsymbol{H}_k)\overline{\boldsymbol{\Phi}}^{(\Phi_{sj})T}] \tag{50}$$

Using (58) in Appendix D with $A = \boldsymbol{Q}$ and $B = \boldsymbol{H}_k$, and noting $\boldsymbol{Q}(\boldsymbol{I}_n - \overline{\boldsymbol{\varphi}}_j\overline{\boldsymbol{\varphi}}_j^T) = \boldsymbol{Q}$,

$$J_{\Phi_{ri}\Phi_{sj}}^{(1)} \sim 2S_e^{-1}\boldsymbol{Q}(r,s)\mathrm{Re}\Sigma\boldsymbol{H}_k(i,j) \tag{51}$$

where $\boldsymbol{Q}(r,s)$ denotes the (r,s)-entry of $\boldsymbol{Q}$; similar notation for $\boldsymbol{H}_k(i,j)$. Assembling $J^{(1)}_{\Phi_{ri}\Phi_{sj}}$ for r and s from 1 to n into a matrix gives the (i,j)-partition of $J^{(1)}_{\boldsymbol{\Phi},\boldsymbol{\Phi}}$:

$$J^{(1)}_{\boldsymbol{\varphi}_i\boldsymbol{\varphi}_j} = 2S_e^{-1}[\mathrm{Re}\Sigma\boldsymbol{H}_k(i,j)]\boldsymbol{Q} \tag{52}$$

Further assembling the partitions for i and j from 1 to m gives the expression in Table 2.

C.3. $J^{(2)}_{\boldsymbol{\Phi},\boldsymbol{\Phi}}$ in Table 2

Using (18) to obtain $\overline{\boldsymbol{\Phi}}^{(\Phi_{ri})}$ and $\overline{\boldsymbol{\Phi}}^{(\Phi_{sj})}$ and substituting into (17),

$$\begin{aligned}
&\text{1st term of } J^{(2)}_{\Phi_{ri}\Phi_{sj}} \\
&= 2N_f tr[\boldsymbol{R}(\boldsymbol{I}_n - \overline{\boldsymbol{\varphi}}_i\overline{\boldsymbol{\varphi}}_i^T)\boldsymbol{e}_r\boldsymbol{e}_i^T\boldsymbol{R}(\boldsymbol{I}_n - \overline{\boldsymbol{\varphi}}_j\overline{\boldsymbol{\varphi}}_j^T)\boldsymbol{e}_s\boldsymbol{e}_j^T] \\
&= 2N_f tr[\boldsymbol{Q}_i\boldsymbol{e}_r\boldsymbol{e}_i^T\boldsymbol{Q}_j\boldsymbol{e}_s\boldsymbol{e}_j^T] = 2N_f tr[\boldsymbol{e}_j^T\boldsymbol{Q}_i\boldsymbol{e}_r\boldsymbol{e}_i^T\boldsymbol{Q}_j\boldsymbol{e}_s] = 2N_f tr[\boldsymbol{e}_r^T\boldsymbol{Q}_i^T\boldsymbol{e}_j\boldsymbol{e}_i^T\boldsymbol{Q}_j\boldsymbol{e}_s]
\end{aligned} \tag{53}$$

where the second equality has used the definition of $\boldsymbol{Q}_i$ in (5). Similarly,

$$\begin{aligned}
&\text{2nd term of } J^{(2)}_{\Phi_{ri}\Phi_{sj}} \\
&= 2\mathrm{Re}tr\Sigma[\boldsymbol{R}^T\boldsymbol{H}_k^{-1}\boldsymbol{R}(\boldsymbol{I}_n - \overline{\boldsymbol{\varphi}}_i\overline{\boldsymbol{\varphi}}_i^T)\boldsymbol{e}_r\boldsymbol{e}_i^T\boldsymbol{H}_k\boldsymbol{e}_j\boldsymbol{e}_s^T(\boldsymbol{I}_n - \overline{\boldsymbol{\varphi}}_j\overline{\boldsymbol{\varphi}}_j^T)] \\
&= 2\mathrm{Re}tr\Sigma[\boldsymbol{e}_s^T(\boldsymbol{I}_n - \overline{\boldsymbol{\varphi}}_j\overline{\boldsymbol{\varphi}}_j^T)\boldsymbol{R}^T\boldsymbol{H}_k^{-1}\boldsymbol{R}(\boldsymbol{I}_n - \overline{\boldsymbol{\varphi}}_i\overline{\boldsymbol{\varphi}}_i^T)\boldsymbol{e}_r\boldsymbol{e}_i^T\boldsymbol{H}_k\boldsymbol{e}_j] \\
&= 2\mathrm{Re}tr\Sigma[\boldsymbol{e}_s^T\boldsymbol{Q}_j^T\boldsymbol{H}_k^{-1}\boldsymbol{Q}_i\boldsymbol{e}_r\boldsymbol{e}_i^T\boldsymbol{H}_k\boldsymbol{e}_j] = 2\mathrm{Re}\Sigma\{[\boldsymbol{Q}_j^T\boldsymbol{H}_k^{-1}\boldsymbol{Q}_i]_{(s,r)}\boldsymbol{H}_k(i,j)\} \\
&= 2\mathrm{Re}\Sigma\{\boldsymbol{H}_k(i,j)[\boldsymbol{Q}_i^T\boldsymbol{H}_k^{-T}\boldsymbol{Q}_j]_{(r,s)}\}
\end{aligned} \tag{54}$$

Combining (53) and (54) and assembling in matrix form for r and s from 1 to n,

$$\begin{aligned}
J^{(2)}_{\boldsymbol{\varphi}_i\boldsymbol{\varphi}_j} &= 2N_f\boldsymbol{Q}_i^T\boldsymbol{e}_j\boldsymbol{e}_i^T\boldsymbol{Q}_j + 2\mathrm{Re}\Sigma\{\boldsymbol{H}_k(i,j)\boldsymbol{Q}_i^T\boldsymbol{H}_k^{-T}\boldsymbol{Q}_j\} \\
&= 2\boldsymbol{Q}_i^T\left[N_f\boldsymbol{e}_j\boldsymbol{e}_i^T + \mathrm{Re}\Sigma\boldsymbol{H}_k(i,j)\boldsymbol{H}_k^{-T}\right]\boldsymbol{Q}_j
\end{aligned} \tag{55}$$

Further assembling the partitions for i and j from 1 to m gives the expression in Table 2.

Appendix D. Some useful identities

For any complex matrix A and Hermitian X,

$$tr[X(A+A^*)] = 2\mathrm{Re}tr(XA) \tag{56}$$

$$tr[X(A+A^*)X(B+B^*)] = 2\mathrm{Re}tr[XBX(A+A^*)] = 2\mathrm{Re}tr[XAX(B+B^*)] \tag{57}$$

For any A ($n\times n$ complex) and B ($m\times m$ complex),

$$tr[A\overline{\boldsymbol{\Phi}}^{(\Phi_{ri})}B\overline{\boldsymbol{\Phi}}^{(\Phi_{sj})T}] = ||\boldsymbol{\varphi}_i||^{-1}||\boldsymbol{\varphi}_j||^{-1}[(\boldsymbol{I}_n - \overline{\boldsymbol{\varphi}}_i\overline{\boldsymbol{\varphi}}_i^T)A^T(\boldsymbol{I}_n - \overline{\boldsymbol{\varphi}}_j\overline{\boldsymbol{\varphi}}_j^T)]_{(r,s)}B(i,j) \tag{58}$$

Eq. (56) was used to simplify (32) and (33). It can be shown as follow:

$$tr[X(A+A^*)] = tr(XA) + tr(XA^*) = tr(XA) + tr(A^*X^*) = tr[XA + (XA)^*] = 2\mathrm{Re}tr(XA) \tag{59}$$

where we have used $tr(XA^*) = tr(A^*X)$ (cyclic property of trace) and $X = X^*$ (Hermitian) in arriving at the second and third equality, respectively.

Eq. (57) was used to simplify (34). It can be shown by noting that $X(A+A^*)X^*$ is Hermitian and applying (56):

$$tr[X(A+A^*)X(B+B^*)] = 2\mathrm{Re}tr[X(A+A^*)XB] = 2\mathrm{Re}tr[XBX(A+A^*)] \tag{60}$$

after using the cyclic property of trace. Swapping A and B and using the cyclic property of trace gives the other equality in (57).

Eq. (58) was used to simplify (50). It can be shown as follow. Using (18) for $\overline{\boldsymbol{\Phi}}^{(\Phi_{ri})}$ and $\overline{\boldsymbol{\Phi}}^{(\Phi_{sj})}$,

$$\begin{aligned}
&tr[A\overline{\boldsymbol{\Phi}}^{(\Phi_{ri})}B\overline{\boldsymbol{\Phi}}^{(\Phi_{sj})T}] \\
&= ||\boldsymbol{\varphi}_i||^{-1}||\boldsymbol{\varphi}_j||^{-1}tr[A(\boldsymbol{I}_n - \overline{\boldsymbol{\varphi}}_i\overline{\boldsymbol{\varphi}}_i^T)\boldsymbol{e}_r\boldsymbol{e}_i^TB\boldsymbol{e}_j\boldsymbol{e}_s^T(\boldsymbol{I}_n - \overline{\boldsymbol{\varphi}}_j\overline{\boldsymbol{\varphi}}_j^T)] \\
&= ||\boldsymbol{\varphi}_i||^{-1}||\boldsymbol{\varphi}_j||^{-1}tr[A(\boldsymbol{I}_n - \overline{\boldsymbol{\varphi}}_i\overline{\boldsymbol{\varphi}}_i^T)\boldsymbol{e}_r\boldsymbol{e}_s^T(\boldsymbol{I}_n - \overline{\boldsymbol{\varphi}}_j\overline{\boldsymbol{\varphi}}_j^T)]B(i,j)
\end{aligned} \tag{61}$$

since $\boldsymbol{e}_i^TB\boldsymbol{e}_j = B(i,j)$, i.e., the (i,j)-entry. Using the cyclic property of trace to move $\boldsymbol{e}_s^T(\boldsymbol{I}_n - \overline{\boldsymbol{\varphi}}_j\overline{\boldsymbol{\varphi}}_j^T)$ to the left,

$$
\begin{aligned}
&tr[A\overline{\boldsymbol{\Phi}}^{(\Phi_{ri})}B\overline{\boldsymbol{\Phi}}^{(\Phi_{sj})T}]\\
&= ||\boldsymbol{\varphi}_i||^{-1}||\boldsymbol{\varphi}_j||^{-1}tr[\boldsymbol{e}_s^T(\boldsymbol{I}_n - \overline{\boldsymbol{\varphi}}_j\overline{\boldsymbol{\varphi}}_j^T)A(\boldsymbol{I}_n - \overline{\boldsymbol{\varphi}}_i\overline{\boldsymbol{\varphi}}_i^T)\boldsymbol{e}_r]B(i,j)\\
&= ||\boldsymbol{\varphi}_i||^{-1}||\boldsymbol{\varphi}_j||^{-1}[(\boldsymbol{I}_n - \overline{\boldsymbol{\varphi}}_j\overline{\boldsymbol{\varphi}}_j^T)A(\boldsymbol{I}_n - \overline{\boldsymbol{\varphi}}_i\overline{\boldsymbol{\varphi}}_i^T)]_{(s,r)}B(i,j)\\
&= ||\boldsymbol{\varphi}_i||^{-1}||\boldsymbol{\varphi}_j||^{-1}[(\boldsymbol{I}_n - \overline{\boldsymbol{\varphi}}_i\overline{\boldsymbol{\varphi}}_i^T)A^T(\boldsymbol{I}_n - \overline{\boldsymbol{\varphi}}_j\overline{\boldsymbol{\varphi}}_j^T)]_{(r,s)}B(i,j)
\end{aligned}
\tag{62}
$$

References

[1] N.M.M. Maia, J.M.M. Silva, Theoretical and Experimental Modal Analysis, Research Studies Press Ltd, Somerset, England, 1997.
[2] D.J. Ewins, Modal Testing: Theory and Practice, Research Studies Press, PA, USA, 2000.
[3] F.N. Catbas, T. Kijewski-Correa, A.E. Aktan (Eds.), Structural Identification of Constructed Systems: Approaches, Methods, and Technologies for Effective Practice of St-Id, American Society of Civil Engineers, 2011.
[4] S.K. Au, F.L. Zhang, P. To, Field observations on modal properties of two tall buildings under strong wind, J. Wind Eng. Ind. Aerodyn. 101 (2012) 12–23.
[5] F.L. Zhang, C.E. Ventura, H.B. Xiong, W.S. Lu, Y.X. Pan, J.X. Cao, Evaluation of the dynamic characteristics of a super tall building using data from ambient vibration and shake table tests by a Bayesian approach, Struct. Control Health Monit. 25 (4) (2017) e2121.
[6] M.J. Glanville, K.C.S. Kwok, Dynamic characteristics and wind induced response of a steel frame tower, J. Wind Eng. Ind. Aerodyn. 54–55 (1995) 133–149.
[7] J.M.W. Brownjohn, E.P. Carden, C.R. Goddard, G. Oudin, Real-time performance monitoring of tuned mass damper system for a 183 m reinforced concrete chimney, J. Wind Eng. Ind. Aerodyn. 98 (3) (2010) 169–179.
[8] A.P. Jeary, Damping measurements from the dynamic behaviour of several large multi-flue chimneys, Proc. Inst. Civ. Eng. 57 (2) (1974) 321–329.
[9] A. DeVivo, C. Brutti, J.L. Leofanti, Modal shape identification of large structure exposed to wind excitation by operational modal analysis technique, Mech. Syst. Sig. Process. 32 (1–2) (2013) 195–206.
[10] J.M.W. Brownjohn, A. Raby, J. Bassitt, A. Antonini, E. Hudson, P. Dobson, Experimental modal analysis of British rock lighthouses, Mar. Struct. 62 (2018) 1–22.
[11] J.M.W. Brownjohn, F. Magalhaes, E. Caetano, A. Cunha, Ambient vibration re-testing and operational modal analysis of the Humber Bridge, Eng. Struct. 32 (8) (2010) 2003–2018.
[12] R. Brincker, M. Lopez-Aenlle, Mode shape sensitivity of two closely spaced eigenvalues, J. Sound Vib. 334 (2015) 377–387.
[13] R. Brincker, Implication of closely spaced modes in OMA, 6th International Operational Modal Analysis Conference, Gijón, Spain, 2015.
[14] W. D'Ambrogio, A. Fregolent, High-order MAC for the correlation of close and multiple modes, Mech. Syst. Sig. Process. 17 (3) (2003) 599–610.
[15] S.K. Au, Fast Bayesian ambient modal identification in the frequency domain, Part I: posterior most probable value, Mech. Syst. Sig. Process. 26 (1) (2012) 60–75.
[16] R. Brincker, C. Ventura, Introduction to Operational Modal Analysis, Wiley, London, 2015.
[17] J.E. Mottershead, C. Mares, S. James, Fictitious modifications for the separation of close modes, Mech. Syst. Sig. Process. 16 (5) (2002) 741–755.
[18] R. Pintelon, P. Guillaume, J. Schoukens, Uncertainty calculation in (operational) modal analysis, Mech. Syst. Sig. Process. 21 (2007) 2359–2373.
[19] E. Reynders, R. Pintelon, G. De Roeck, Uncertainty bounds on modal parameters obtained from stochastic subspace identification, Mech. Syst. Sig. Process. 22 (2008) 948–969.
[20] M. Döhler, X.B. Lam, L. Mevel, Uncertainty quantification for modal parameters from stochastic subspace identification on multi-setup measurements, Mech. Syst. Sig. Process. 36 (2013) 562–581.
[21] S.K. Au, Operational Modal Analysis: Modelling, Inference, Uncertainty Laws, Springer, Singapore, 2017.
[22] S.K. Au, Fast Bayesian ambient modal identification in the frequency domain, Part II: posterior uncertainty, Mech. Syst. Sig. Process. 26 (1) (2012) 76–90.
[23] S.K. Au, J.M.W. Brownjohn, J.E. Mottershead, Quantifying and managing uncertainty in operational modal analysis, Mech. Syst. Sig. Process. 102 (2017) 139–157.
[24] Y.C. Ni, X.L. Lu, W.S. Lu, Operational modal analysis of a high-rise multi-function building with dampers by a Bayesian approach, Mech. Syst. Sig. Process. 86 (2017) 286–307.
[25] H.F. Lam, F.L. Zhang, Y.C. Ni, J. Hu, Operational modal identification of a boat-shaped building by a Bayesian approach, Eng. Struct. 138 (1) (2017) 381–393.
[26] H.R. Pan, Z.N. Xie, A. Xu, L. Zhang, Wind effects on Shenzhen Zhuoyue Century Center: field measurement and wind tunnel test, Struct. Des. Tall Special Build. 26 (13) (2017), https://doi.org/10.1002/tal.1376.
[27] P. Liu, P.Y. Lian, W.G. Yang, Horizontal resonance of a 13 story building under external machine vibrations, J. Struct. Stab. Dyn. 18 (1) (2018) 1850005.
[28] S.K. Au, B.B. Li, Posterior uncertainty, asymptotic law and Cramer Rao Bound, Struct. Control Health Monit. 25 (3) (2017), https://doi.org/10.1002/stc.2113.
[29] Y.L. Tong, The Multivariate Normal Distribution, Springer, New York, 1990.
[30] R.A. Horn, C.R. Johnson, Matrix Analysis, Cambridge University Press, UK, 2013.
[31] M. Brookes, The Matrix Reference Manual, 2011. http://www.ee.imperial.ac.uk/hp/staff/dmb/matrix/intro.html.